


INFLUENCE OF CANTOR ALLOY PARTICLES ON MICROSTRUCTURE, AND WEAR BEHAVIOR OF ALUMINUM METAL MATRIX COMPOSITE

Akshay Kumar , Alok Singh, Amit Suhane and Pradip Kumar Verma

Department of Mechanical Engineering, Maulana Azad National Institute of Technology, Madhya Pradesh, Bhopal 462003, India

Ashish Kumar Singh

Department of Materials Engineering, Indian Institute of Science, Bangalore, Karnataka 560012, India

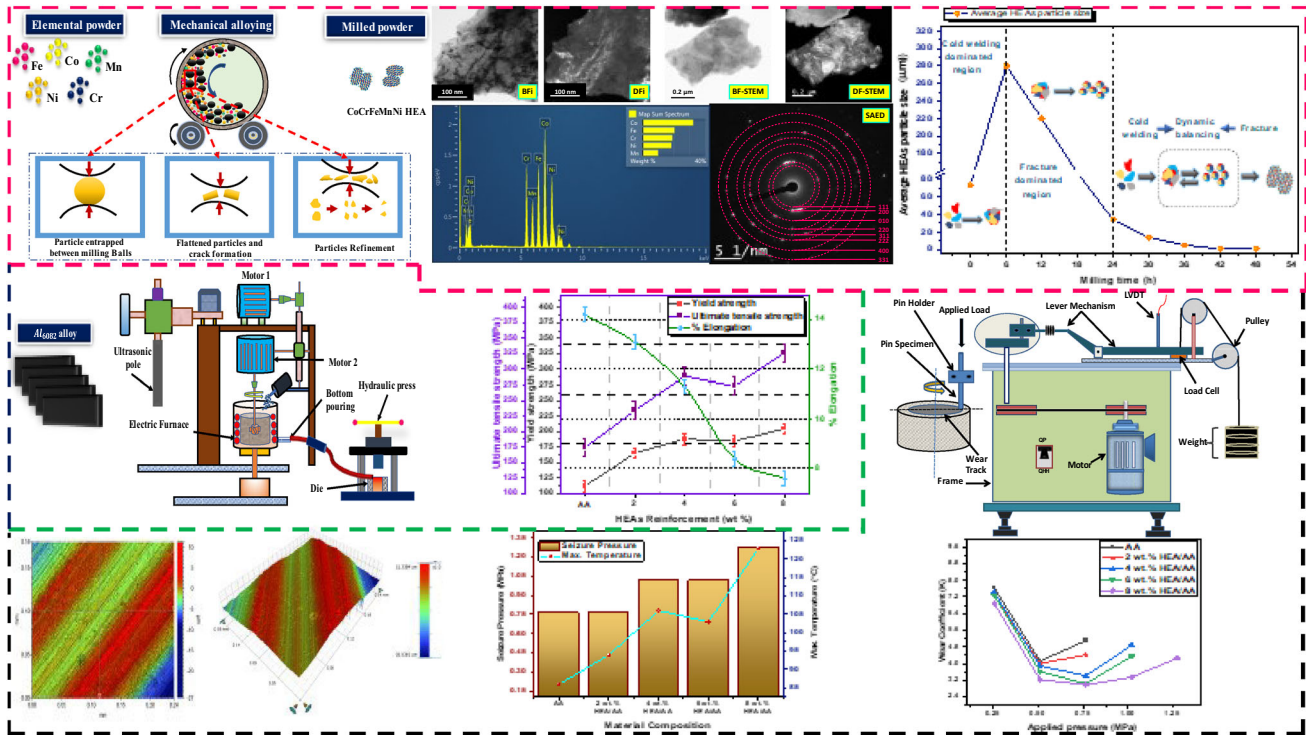
Copyright © 2023 American Foundry Society
<https://doi.org/10.1007/s40962-023-01099-2>

Abstract

The performance of industrial tribo-systems depends on advanced composites with superior tribological characteristics. In this study, the CoCrFeMnNi high entropy alloy (HEA) is prepared through mechanical alloying, while stir squeeze casting aided with an ultrasonic transducer is used to fabricate AA 6082 alloy and x% HEA/AA composites (where, x= 2, 4, 6, 8 in weight percentage). The effect of HEA_p on dry sliding wear performance of HEA/AA composites is examined in as-cast conditions using a pin-on-disk wear tester at varying normal applied pressure (0.254 MPa, 0.509 MPa, 0.763 MPa, 1.018 MPa, and 1.273 MPa), varying sliding distance (1000 m, 2000 m, 3000 m, 4000 m, and 5000 m) and a constant sliding speed (3.5 m/sec), special emphasis is centered on response factors such as wear rate, seizure resistance, and bulk temperature

upsurge. The composite showed an ability to withstand higher temperatures, and better seizure and wear resistance over the alloy. The phase identification and microstructural study were carried out using an X-ray diffractometer, field emission scanning electron microscope, and transmission electron microscope, whereas the topography of worn-out surface was examined through an optical profilometer. There was a substantial decrease in coefficient of friction, and wear rate noticed as the HEAs concentration increased, whereas in all the wear conditions, the wear rate of 8% HEA/AA composite shows maximum resilience against wear, the inclusion of HEA particles also influences the extent of the subsurface at the seizure condition.

Graphical Abstract



Keywords: aluminum metal matrix composite, high entropy alloy, mechanical alloying, stir-squeeze casting, tribological behavior, fracture mechanism, wear sub surface

Introduction

The utilization of aluminum metallic composites has gained popularity due to their superior mechanical characteristics, such as high modulus,¹ high stiffness,² and unique strength. With the capability to withstand elevated temperatures, low thermal expansion, high wear resistance,^{3,4} and high damping capacity, they are poised to meet the demands of rigorous industrial applications.^{5,6} This has resulted in increased research and development into metallic composites as a new and innovative class of materials. The full potential of these materials can only be realized through a synergistic approach that enhances the properties of both the reinforcement and matrix. Aluminum metallic composites (AMCs) have emerged as a promising candidate for a range of industries, including the automotive sector, energy industry, aviation sector, defense sector, trusses and bridges, and other engineering applications.⁷⁻⁹

In recent years, significant research has been conducted on Al alloys (6000 series) for both structural and industrial applications. However, a major challenge with these alloys

is their poor weldability with similar and dissimilar materials. As a result, they are often joined through riveting or bolting, making them more susceptible to vibrations and leading to fretting and sliding wear in dry ambient conditions.^{10,11} This demands further investigation into the tribological behavior of Al alloy systems.¹¹ The Al6082 alloy (Al-Mg-Si series), one of the most widely discussed alloys along with 6061 and 6063, has the benefits of medium strength, better weldability, and resistance to wear and corrosion and is widely adopted in the automobile,¹² marine, aviation, and structural industries.^{13,14}

Reinforcements in AMCs include TiC, TiB₂, Mg₂Si, SiC, WC, and others. However, in recent times, HEAs have gained attention due to their unique properties and are reported to be used as reinforcement in WC, Cu, Fe, and Ti matrix composites. Wear resistance can be greatly improved by incorporating a new design approach.¹⁵ This new method of alloy design introduces a new aspect to the discipline of materials science.¹⁶ High-entropy alloys (HEAs) comprise a minimum of five primary elements in equimolar proportions, with no apparent differentiation

between solvent and solute.^{17,18} The conventional alloys previously utilized as reinforcing agents have limited combinations that possess a single-phase solid solution capable of exhibiting specific physical and mechanical properties. An exemplary illustration of such a single-phase face-centered cubic (fcc) solid solution is found in a Cantor alloy known as “CoCrFeMnNi.”¹⁹ Previous research studies on CoCrFeMnNi have revealed intriguing characteristics, including an enhanced yield strength at significantly reduced temperatures, particularly under cryogenic conditions. This behavior was previously observed only in body-centered cubic (bcc) metals and a few binary phase fcc metals. Furthermore, it is evident that the Cantor alloy system not only enhances strength but also increases the percentage elongation (ductility) at lower temperatures.²⁰ Numerous studies have been conducted to comprehensively investigate the Cantor alloy. Gao et al.²¹ processed a CoCrFeMnNi High-Entropy Alloy (HEA) that exhibited exceptional properties, such as a high percentage elongation (57%) and ultimate tensile strength of 620 MPa. Chew et al.²² reported remarkable properties of the CoCrFeMnNi HEA, with a yield strength of 518 MPa and an ultimate tensile strength of 660 MPa.

Thus, it has been observed that HEA particles have proven to be a better candidate for reinforcing agents. Kumar et al.²³ investigated the effect of HEA particulate reinforcement in 2024 aluminum and found that the composite had improved mechanical properties such as hardness (102 HV), Young modulus (102.69), yield strength (405 MPa), and tensile strength (563.65 MPa) owing a smooth interface that allowed for effective load transfer and prevented reinforcement particle agglomeration. Junchen et al.²⁴ developed a novel AMC-reinforced Al_{0.8}CoCrFeNi HEA_p and stated that HEA_p uniformly distributed and maintained structural integrity. Interfacial bonding was observed due to the formation of Al₃CoCrFeNi instead of intermetallic phases that impart high yield strength (200) and ultimate tensile strength (371MPa).

The optimal combination of hard and soft phases offers a combination of better fracture toughness, higher strength, and improved wear resistance.^{25,26} Soft particulates enhance resistance against wear by acting as a self-lubricating film between contacting surfaces but reducing the hardness of the composite.^{27,28} Hence, a combination of hard dispersoids with soft particulates effectively improves the hardness and wear resistance of the composite.^{29,30} In this context, CoCrFeMnNi is notably a potential candidate

due to its superior properties such as better elastic modulus, better hardness, good oxidation and corrosion resistance, high thermal stability, and improved wear resistance.^{31–33} HEAs have been reported to exhibit good wettability with metals, facilitating improved densification.^{34,35}

The development of composite via stir casting is the most intricate part for uniform distribution of sub-micron and nanoparticles in aluminum matrix composite.³⁶ A comparable high difference in densities between matrix and reinforcement, and high specific surface area of nano and submicron size particles raises the wettability issue.^{37,38} To overcome this issue, stir casting assisted with an ultrasonic transducer is utilized by many researchers. The molten metal stirrer is mechanically for uniform distribution of reinforcement particles subjected to ultrasonic cavitation that breaks agglomeration and clustering of particles and uniform dispersion of HEA particles before being poured into the die.^{39,40}

The overview of this research article can be structured as:

- In this study, the authors developed a novel composite with unique composition in the quest to obtain superior mechanical and wear-resistant properties that can replace the existing alloy. A CoCrFeMnNi HEA reinforced -AA 6082 composite tailored and produced through stir casting with the aid of ultrasonic transduction. The CoCrFeMnNi HEA is processed through mechanical alloying as it has better control over the morphology and microstructure of HEA particles.
- The microstructural examination, along with the mechanical and wear properties, was performed to comprehensively evaluate the tribological behavior of the HEA-reinforced aluminum metallic composites.
- The impact of applied pressure on both the wear surface and subsurface was analyzed using optical profilometry, FESEM, and wear mapping was generated from the experimental data to gain deeper insight into the wear behavior.

Experimental Procedure

An experimental investigation was conducted to examine the properties of an AA 6082 aluminum matrix composite that was reinforced with various concentrations of high entropy alloy (HEA) particles. AA 6082 alloy in the form

Table 1. Elemental Composition of AA-6082

Elements	Mn	Cr	Zn	Si	Mg	Cr	Fe	Cu	Ti	Al
Wt.%	0.55	0.02	0.01	0.92	0.92	0.02	0.29	0.04	0.01	Rest

of cylindrical bars was processed and as-cast alloys and composite were obtained in finger shape that was processed further and desired specimen and dimension were achieved. Energy dispersive X-ray spectroscopy (EDS) was used to determine the elemental composition of AA 6082 i.e., listed in Table 1.

Processing of CoCrFeMnNi HEA

The HEA reinforcement was synthesized via mechanical alloying, utilizing equiatomic elemental powders (Ni, Co, Fe, Cr, Mn) of particle size 60 μm and a purity level of 99.5%. Mechanical alloying was used to process HEA particles which were carried out in a vertical planetary ball mill in which balls and a flask were used that made up of tungsten carbide material. A small quantity i.e., 1.5 wt% toluene was used as the process control agent. The charge-to-ball weight ratio was used as 1:10 whereas, the rotating speed was set as 300 RPM. Powder samples were collected at 6-hour intervals to monitor the degree of milling, and after 42 hours, all HEA particles were collected for further processing.

Processing of As-Cast AA 6082 and Composites

The preparation of the alloy and composite specimens was carried out using a stir-squeeze casting process in conjunction with an ultrasonic transducer (Figure 1). The AA 6082 matrix was heated to 720 $^{\circ}\text{C}$ in a resistance furnace. To prepare the CoCrFeMnNi HEA reinforcement particles, they were preheated in a muffle furnace at 150 $^{\circ}\text{C}$ to remove moisture and avoid abrupt temperature changes during mixing. Coverall-11 flux was added to the molten matrix to remove impurities, and purging was applied to prevent unwanted reactions. Stirring was performed for 5 minutes at 400 RPM to create a vortex flow for the homogeneous distribution of the reinforcement particles. To prevent particle agglomeration, an ultrasonic transducer probe was employed at 20 KHz for 8 minutes. The molten mixture was then squeezed into a preheated permanent mold through a runner, with a load of 120 MPa applied via the hydraulic press.

Microstructural Characterization Techniques

The phase composition of the CoCrFeMnNi high entropy alloy (HEA) powder particles and composites were analyzed using X-ray diffraction (XRD) on a Rigaku XRD instrument operating at room temperature and utilizing a Cu-K α wavelength of $\lambda = 0.15406$ nm with an operating voltage of 40 kV and current of 40 mA. The step size, scan speed, and diffraction angle range were 0.02, 5 $^{\circ}$ /min, and 10–100 $^{\circ}$, respectively. The XRD pattern was analyzed

using X'pert High Score software and was used to determine the phases present, evaluate lattice stress and strain, and estimate crystallite size. The microstructure and interface of the HEA particles and aluminum matrix were characterized using Nova Nano FESEM 450 (FEI) with energy dispersive X-ray spectroscopy (EDS), and elemental mapping was performed to investigate the distribution of elements in the sample and analysis of wear surface. The magnification used for analysis varied between 20,000x and 500x i.e., 20,000x, 3500x, 2000x, 1000x, and 500x for scales of 5 μm , 30 μm , 50 μm , 100 μm , and 200 μm . For the FESEM analysis, a 10 mm diameter having thickness 10 mm sample is prepared, which is subjected to a polishing process (utilizing different grit size emery paper i.e., 400, 600, 800, and 1200) followed by cleaning and wet cloth polishing using alumina paste carried out, including cleaning with an ultrasonicator and etching (a Keller's reagent etching) for 8 seconds under ambient conditions, to prepare them for examination. The nanocrystalline nature of the mechanically alloyed CoCrFeMnNi HEA powder particles was examined using transmission electron microscopy (TEM) on a JEOL JEM 300 FS instrument operating at 300 kV. The powder was sonicated in ethanol to prevent agglomeration and was mounted on a gold-coated grid for analysis. The aluminum alloy and composite specimens were prepared using a diamond cutter to obtain thin slices, which were then polished and ultrasonicated in ethanol to remove surface debris. The specimens were perforated using TenuPol-5 twin-jet electropolishing and post-ion polished using Gatan Pips II 695 ion beam milling. The samples were examined through the TEM.

Density Measurement

Density measurements were conducted on cast materials in accordance with ASTM C693 standards. The water displacement method was utilized to adhere to Archimedes' principle. The porosity present in the casted material was calculated using the pertinent Eqn. 1.

$$\text{porosity}\% = \left[\left(\frac{\rho_{\text{th}} - \rho_m}{\rho_m} \right) \right] \times 100 \quad \text{Eqn. 1}$$

Where, ρ_m was the measured density (actual) and ρ_{th} was the theoretical density. A precise measurement using the Archimedean principle revealed the actual density. The theoretical densities derived from the mixing law were evaluated by the following expression as in Eqn. 2:

$$\rho_{\text{th}} = (\rho_{\text{Al}} \times w_{\text{th}}) + (\rho_{\text{HEA}} \times w_{\text{HEA}}) \quad \text{Eqn. 2}$$

Where, ρ_{th} , ρ_{Al} , ρ_{HEA} , and w_{th} were the theoretical density of composite, the density of matrix alloy, the density of HEA, and reinforcement concentration. Here, the ρ_{Al} was 2.71 g/cm 3 and the ρ_{HEA} was 7.88 g/cm 3



Figure 1. Stir-squeeze casting setup assisted with an ultrasonic probe.

Hardness Measurement

The hardness of the polished surfaces of the as-cast alloys and composites was evaluated through Digital Rockwell Tester (Model: RANSE-1, made by FIE) in accordance with ASTM E-18 standard. A 1/16" steel ball indenter was used to apply a 100 N load for 10 seconds to the specimens, utilizing the B scale. To minimize the likelihood of indenter effects on the HEA reinforcement particles, the hardness tests were precisely carried out at 10 distinct locations and the average of the 10 readings was determined.

Tensile Test

The tensile testing of HEA-reinforced aluminum metal matrix composite was conducted on the universal testing machine that revealed properties such as ductility (% elongation), yield strength, and ultimate tensile strength. The ASTM E-8 M standard was used for the tensile test of AMCs and to achieve better accuracy in the result three specimens of a composition were tested and their average values were reported (Figure 1).

Dry Sliding Wear

The tribological properties of the composites were investigated over dry sliding tests at various concentrations of HEA reinforcement, applied loads, and sliding distances. The tests were conducted on a Ducom TR-201 CL Pin-on-Disk Wear Apparatus, in accordance with G99-95 ASTM

standard and the schematic diagram is shown in Figure 2. Specimens with a diameter of $\varnothing = 10$ mm and a height of $h = 35$ mm were fabricated from the composites for the wear tests. The sliding surfaces of the pins were carefully polished with emery paper and cleaned with ethyl alcohol before testing. To minimize measurement error, three composite samples were tested for each reinforcement condition. After each test, the track surface of the disk was thoroughly cleaned with acetone to eliminate any adhesion of wear debris. The weight loss was determined using an electronic microbalance with an accuracy of ± 0.01 mg by comparing the weight of the specimen before and after the test. The test was performed for a sliding distance of 6000 m or until melting or seizure was observed, indicated by intense vibration, an unpleasant noise, and an abrupt temperature rise. The pressure and sliding distance were recorded at the moment of seizure to assess the wear response parameters. These parameters are listed in Table 2.

A weight loss approach was employed to determine the dry sliding wear rate of the fabricated alloy and composite, which was then represented as volumetric loss per unit sliding distance (mm^3/m). A type K bare thermocouple tip was placed into a 2 mm diameter hole on the pin sample's lateral surface, 2 mm distant from the contact zone, to measure temperature. The pin samples were held in such a way that a 4 mm portion of it protruded from the sample holder. It is important to note that the temperature readings obtained during these tests represent the temperature at the location of the thermocouple, and the actual temperature in the contact zone may be higher than the obtained values.

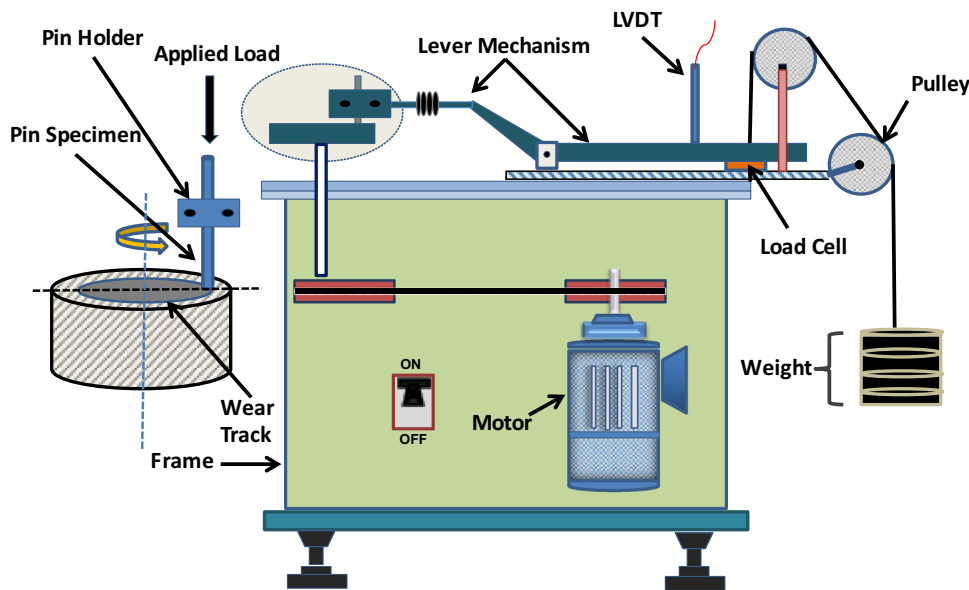


Figure 2. Schematic diagram of dry sliding wear machine.

Table 2. Details of Wear Test Parameters

S.No.	Wear test attributes	Parameter values
1.	Ambient temperature	27–29 °C
2.	Humidity	65–70%
3.	Cylindrical pins dimension	$\phi 10 \times 35 \text{ mm}^2$
4.	Counter disk material	EN-32 Grade steel
5.	Track diameter	80 mm
6.	Sliding speed	400 RPM (fixed)
7.	Normal applied Pressure	0.25, 0.50, 0.76, 1.1, 1.27 MPa
8.	Sliding distance	5000 m (fixed)

Results

Characterization of HEA Powder Particles

The X-ray diffraction (XRD) pattern of equiatomic CoCrFeMnNi high entropy alloys (HEA) particles, which were processed through mechanical alloying. The XRD pattern of the raw material prior to milling exhibits peaks corresponding to all constituent elements, as shown in Figure 3. As milling time increases, the peaks of the constituent elements decrease in intensity and broaden, and eventually disappear in the order of their melting points, as demonstrated by the XRD pattern. For example, the peak of Mn disappears at 6 hours of milling time, followed by Ni, Co, Fe, and Mn, which disappear at 12, 18, 24, and 36 hours of milling time, respectively. At 36 hours of milling time, almost all peaks have disappeared and the face-centered cubic (FCC) phase is confirmed. The observed dissolution order is consistent with prior studies and aligns with the melting points of the constituent elements, where lower melting points correspond to higher dissolution.⁴¹

The microstructure and morphology of the CoCrFeMnNi HEA at 42 hours are depicted in Figure 4a–c. Elemental mapping and EDS analysis were conducted to confirm the distribution and concentration of different elements in the HEA powder particles.

Milling was categorized into three zones based on particle size, morphology, and microstructure, as shown in Figure 4d. The first zone, from 0 to 6 hours, was characterized by cold welding and plastic deformation, resulting in an increase in particle size from 80 to 282 μm , and an irregular shape was observed. The second zone, from 6 to 24 hours, was characterized by the refinement of grain and increased lattice strain due to atom diffusion and dissolution⁴² and the particles get finer however rod shape and flat plate particles were noticed. The third zone, after 42 hours of milling, was characterized by a dynamic equilibrium between cold welding and fracturing, with an average particle size of 0.8362 μm , and the different size particles with nearly spheroidal and some round flattened shape particles were prominent. Beyond 42 hours of milling, the powder was negatively impacted, resulting in difficulties in phase identification and contamination issues.⁴³

Figure 5a, b illustrates the bright field and dark field HRTEM image, whereas 5 (c) and 5 (d) show the bright field and dark field STEM image of 42 hr milled CoCrFeMnNi HEA particles with a corresponding selected area electron diffraction (SAED) through Figure 5f. The SAED of the milled HEA particle confirms the formation of FCC phase HEA. TEM assisted with EDX was used to examine the distribution of elements in the particle for accurate study (Figure 5E). A large particle was chosen in the TEM grid and observed that all the elements Cr, Co, Ni, Mn, and Fe were evenly distributed.

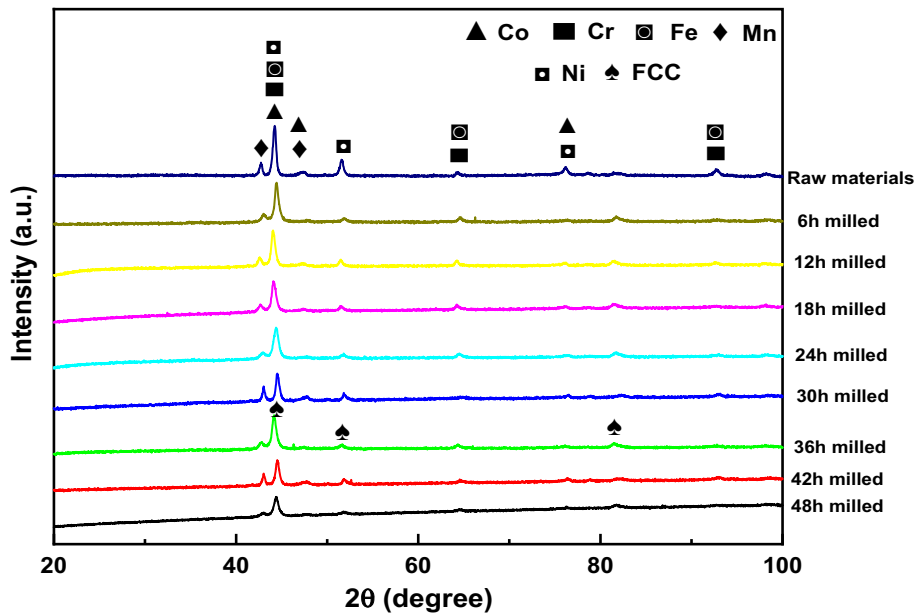


Figure 3. XRD pattern of HEA powder particle for different milled time.

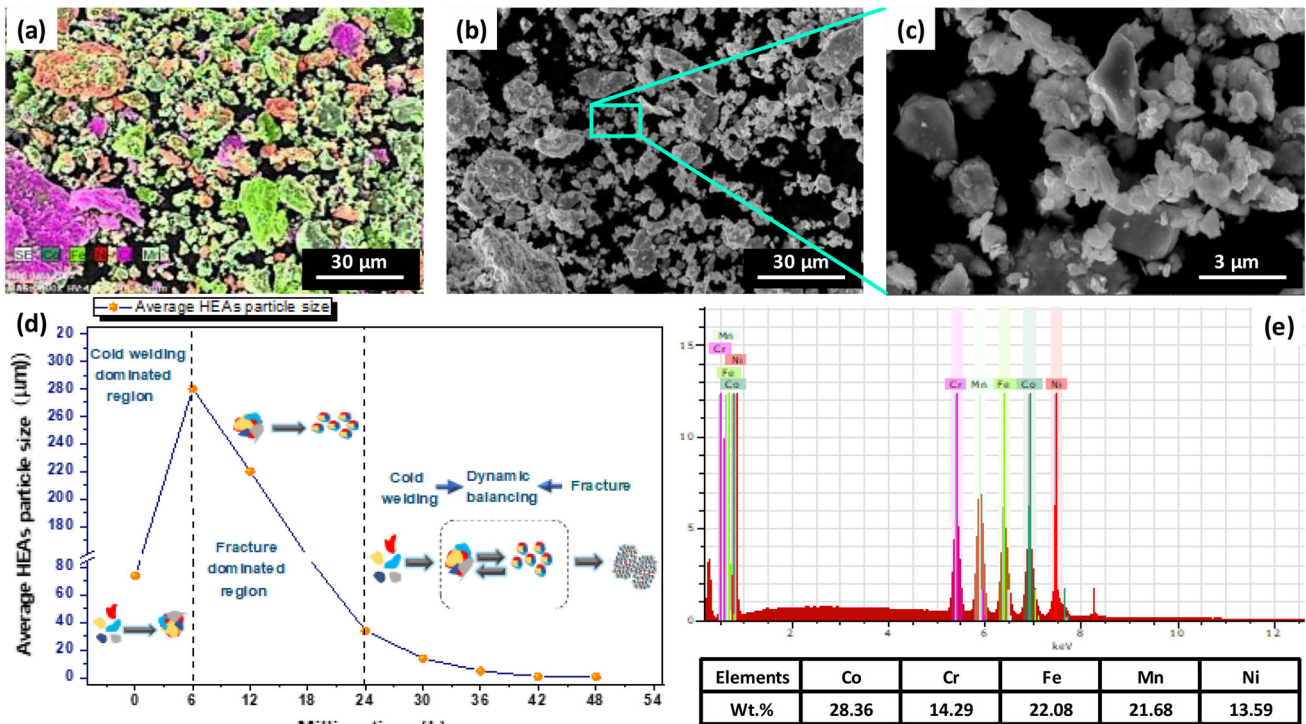


Figure 4. 42 hr milled powder: (a) elemental mapping; (b, c) particle morphology at low magnification and high magnification FESEM images; (d) particle size variation with milling time (e) Cross-sectional EDS of a figure (b).

Microstructural Analysis of Alloy and Composites

The microstructural study of the as-cast 6082 AA and HEA/AA composite revealed the formation of the α -Al phase and the presence of CoCrFeMnNi HEA particles, in addition to the formation of various intermetallic phases. The nucleated intermetallics exhibited different geometric

shapes, such as a polyhedron, round (plate-form), and rod shapes, as confirmed by XRD diffractogram analysis. The investigation of different intermetallics phases in the etched specimens of the alloy and composite was carried out using optical microscopy, in combination with XRD pattern analysis (Figure 6). The study revealed that Keller reagents are capable of imparting distinct colors to different intermetallics, including α -Al(FeMn)Si (dark phases),

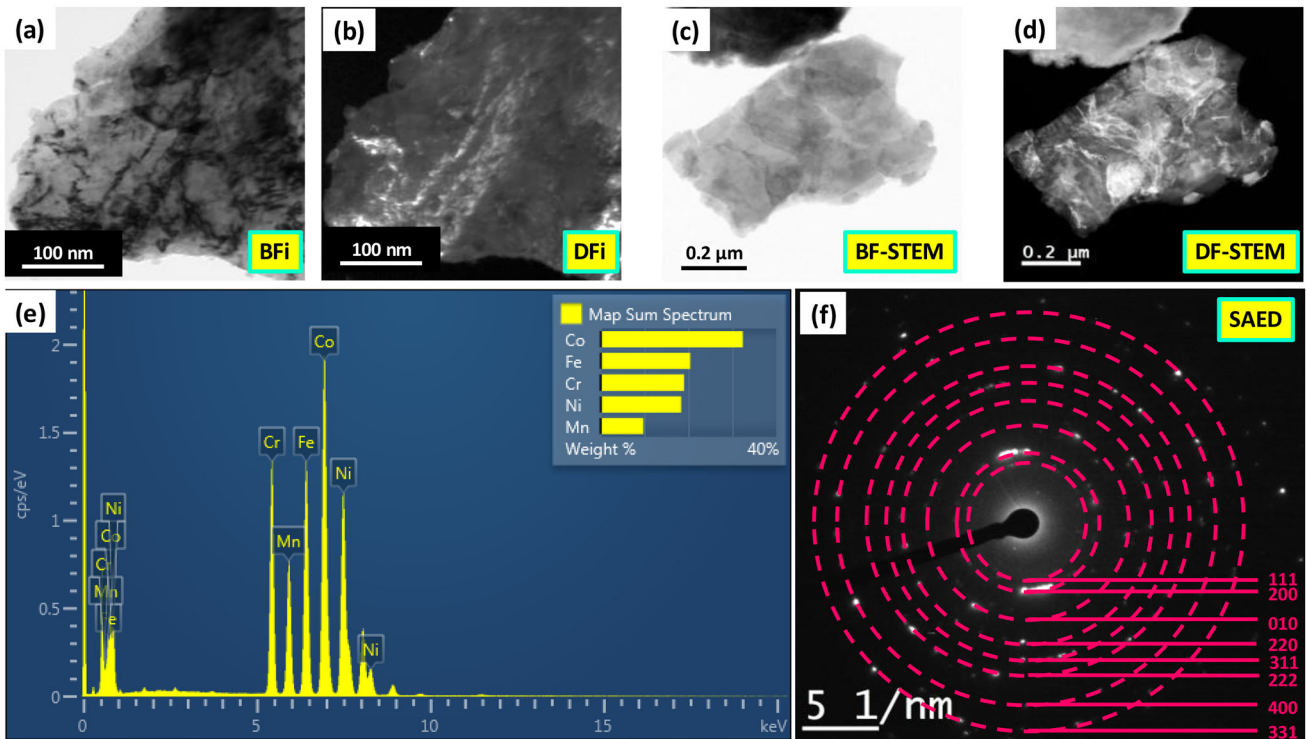


Figure 5. TEM analysis of 42 hr CoCrFeMnNi HEA particle: (a) bright-field HRTEM image; (b) dark-field HRTEM image; (c) bright-field STEM image; (d) dark-field STEM image; (e) EDS analysis of STEM HEA particles; (f) Selected area electron diffraction analysis.

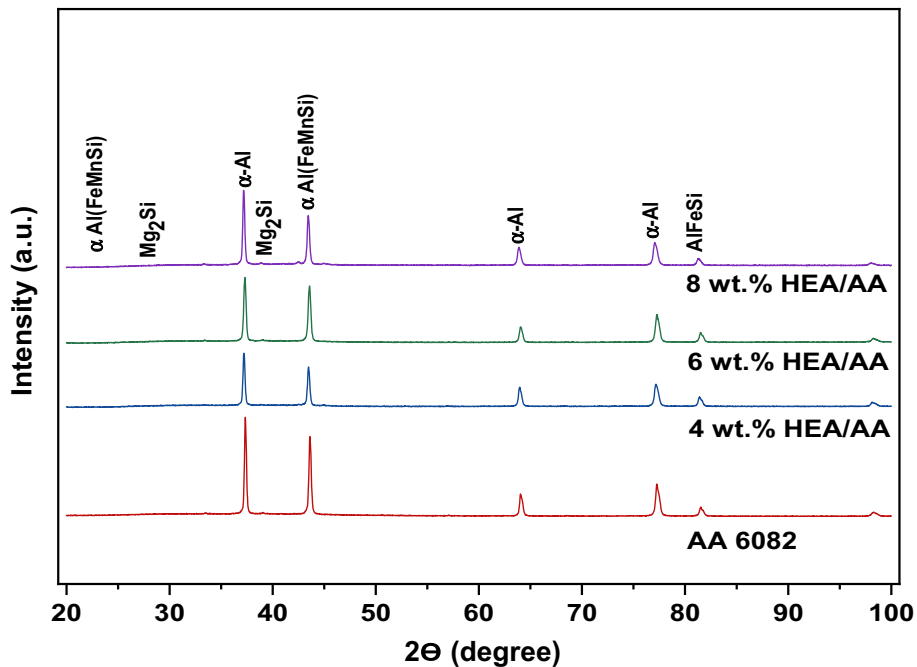


Figure 6. XRD diffractogram of AA6082 and HEA/AA6082 composites.

β - Al_3FeSi (gray phases), and Mg_2Si (black phases), as depicted in Figure 7. The evolution of solute intermetallic phases resulted from eutectic or peritectic reactions that took place during the solidification of the solid solution.⁴⁴⁻⁴⁶ The cluster of α - $\text{Al}(\text{FeMn})\text{Si}$ solute eutectic

intermetallics formed near and at grain boundaries can be observed in Figure 7vi. Plate-form β - Al_3FeSi intermetallics are typically reported in the inter-dendritic zone (Figure 7vii), while Mg_2Si (black phases) intermetallics are

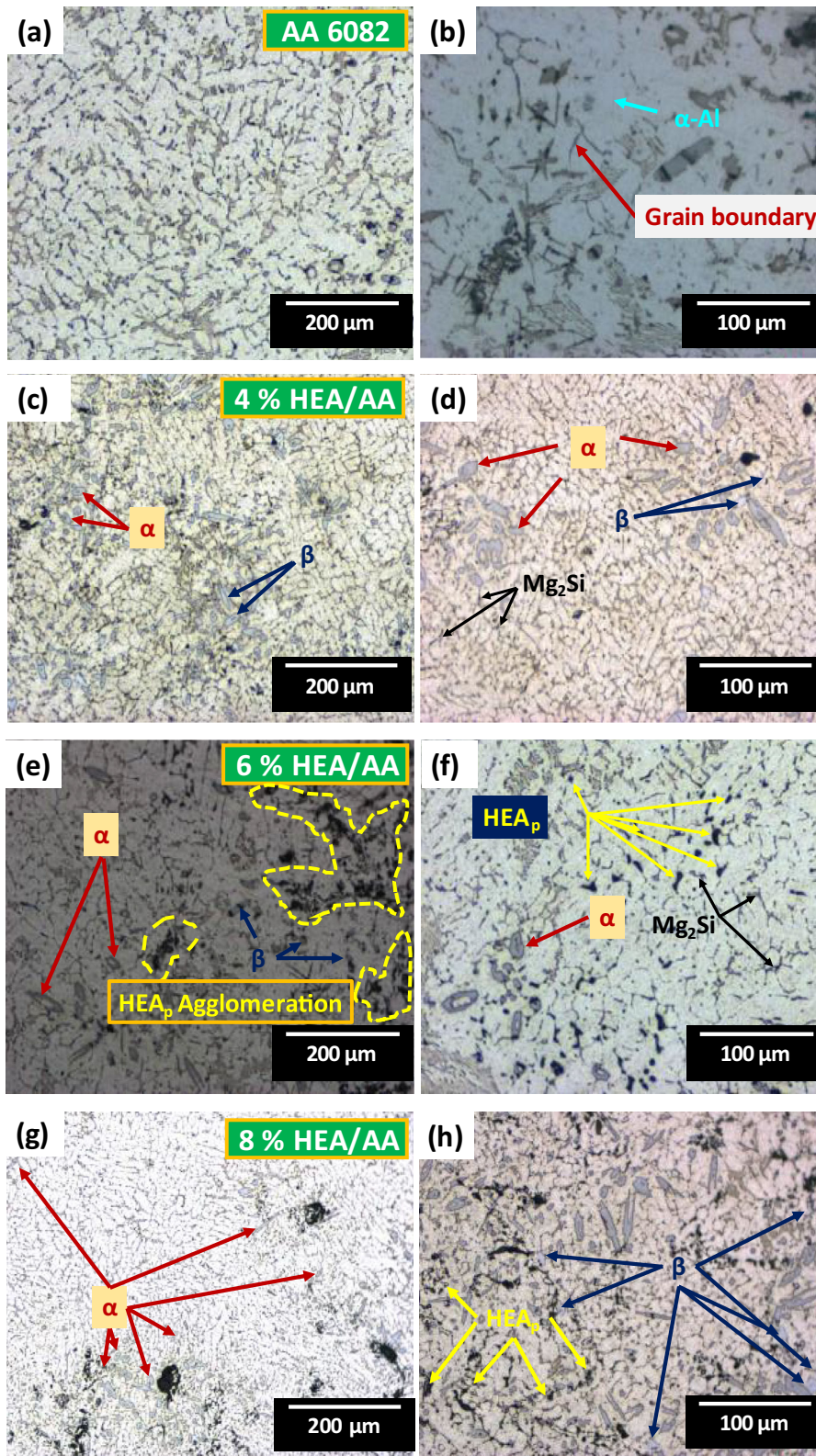
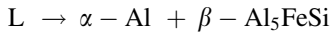


Figure 7. Optical microscope images: (a, b) low and high magnification images of AA 6082; (c, d) low and high magnification images of 4% HEA/AA composite; (e, f) low and high magnification images of 6% HEA/AA composite; (g, h) low and high magnification images of 8% HEA/AA composite.

noticeable at grain boundaries in Figure 7ii, Figure 7vi, and Figure 7x.



The morphological Structures of different intermetallics phases are very intricate so along with optical microscopy FESEM with EDS is used to differentiate among different phases.

The dispersion of HEA particles in the aluminum matrix was analyzed using FESEM on the produced samples. Figures 8 display the FESEM microstructure of as-cast

alloy and composite samples containing HEA concentrations of 2%, 4%, 6%, and 8%, respectively. The uniform distribution of HEA particles was confirmed, with a few instances of clustering observed. However, the use of ultrasonic transducer-generated cavitation broke apart these clusters. Optical microscope images and FESEM images disclosed the microstructure and average grain size of the cast aluminum and HEA reinforcement composite. The grain size was estimated in accordance with ASTM E112-17a using the line intercept approach, and the results showed that the inclusion of HEA particles refined the grain structure and reduced the average grain size from 131.089 μm in 6082 AA to 51.6486 μm in 2% HEA/AA composite. The average grain size was further reduced to 24.184 μm in the 4% HEA/AA composite. In the 6% HEA/

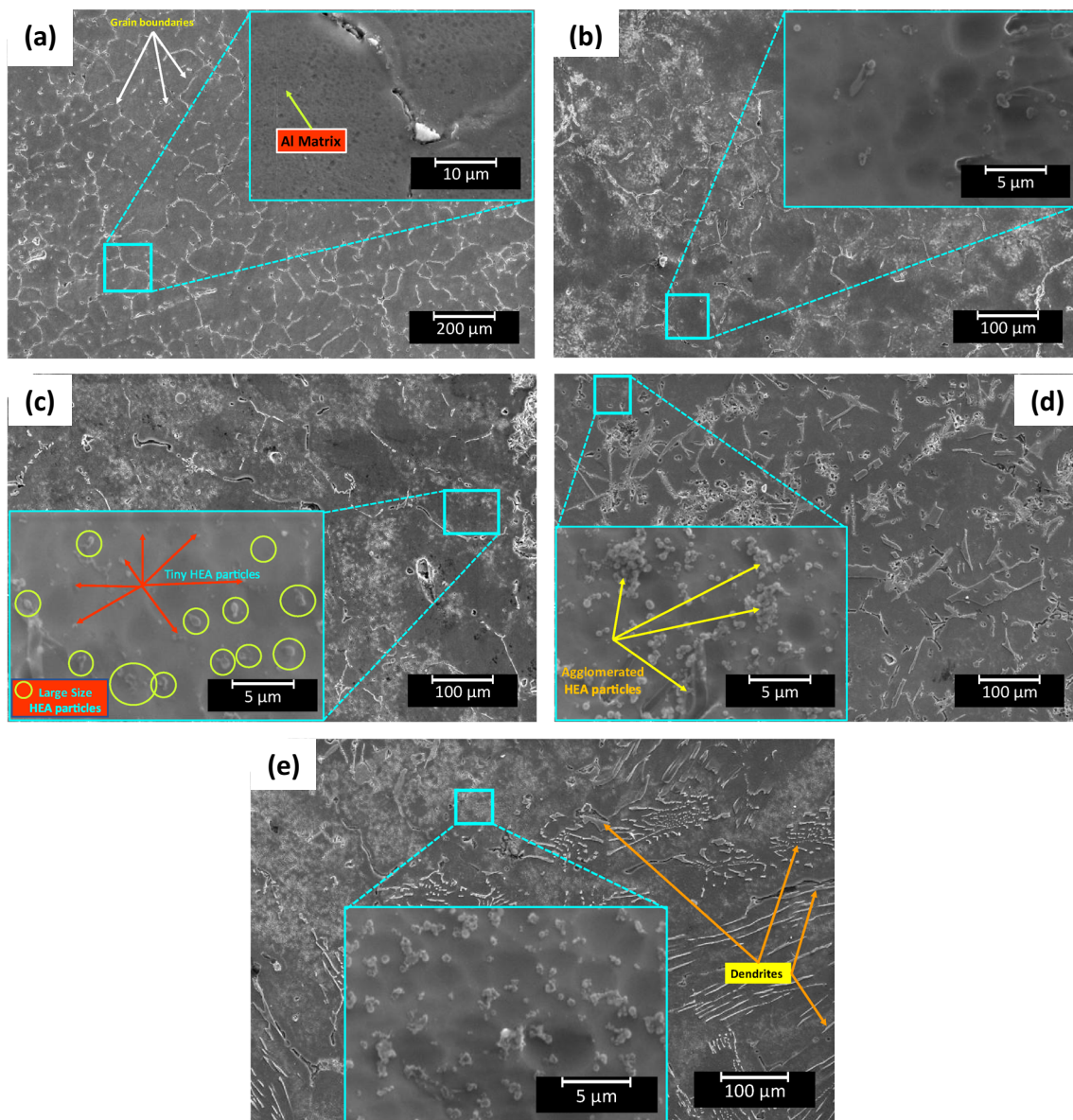


Figure 8. FESEM images: (a) As-cast AA 6082, (b) 2% HEA/AA, (c) 4% HEA/AA, (d) 6% HEA/AA, (e) 8% HEA/AA.

Table 3. Elemental Composition of AA 6082 Alloy and HEA/AA Composites

Figures	Elements										
	Al	Mg	Si	Mn	Zn	Fe	Cu	Cr	Ti	Co	Ni
Figure 8a	95.49	2.45	0.56	0.50	0.35	0.36	0.19	0.04	0.06	–	–
Figure 8b	94.78	1.52	1.19	0.64	0.47	0.44	0.15	0.09	0.03	0.09	0.57
Figure 8c	94.40	1.61	1.19	0.71	0.48	0.63	0.21	0.11	0.04	0.11	0.51
Figure 8d	92.23	2.30	1.53	0.40	0.62	0.45	0.34	0.23	0.21	0.39	1.30
Figure 8e	91.46	1.31	0.91	0.74	0.75	1.21	0.63	0.46	0.11	1.26	1.15

Table 4. Variation of Physical Properties with Varying HEA Concentration

S.No.	Composition	AA 6082 (wt%)	CoCrFeMnNi HEA (wt%)	Theoretical density (g/cm ³)	Measured density (g/cm ³)	Porosity (%)
1.	AA 6082	100	0	2.710	2.680	1.110
2.	2% HEA/AA	98	2	2.813	2.770	1.560
3.	4% HEA/AA	96	4	2.916	2.878	1.348
4.	6% HEA/AA	94	6	3.020	2.948	2.440
5.	8% HEA/AA	92	8	3.123	3.072	0.016

AA composite, HEA particle agglomeration was observed, as shown in Figure 8iv, and the average grain size was reported as 31.892 μm . In the 8% HEA/AA composite, uniform distribution of HEA particles was observed, as shown in Figure 7v, and the grain size was reported as 12.897 μm . The variation of elemental composition in alloy and composites of Figure 8 listed in Table 3.

Physical Properties

Density and Porosity

The variation of density and porosity with HEA content is listed in Table 4. The trend of density and porosity curve revealed that irrespective of HEA content theoretical densities were lowered than measured densities of as-cast alloy and composites. The density of the composite increased with HEA content and the maximum value was reported for 8% HEA/AA composite. Although a density of 6% HEA/AA composite is inconsistent with the trend and the reported value is lower than 4% HEA/AA composite. The possible factors that contribute were: (i) gas trapped during solidification, (ii) particle segregation, (iii) casting defects, and (iv) evolution of H_2 .

The density of a composite affects its overall weight and can influence its mechanical properties. Higher density often correlates with higher strength in AMMCs. A denser composite typically has a high load-bearing capacity and

provides resistance to any deformation under applied loads. High-density materials exhibit higher stiffness leading to increased rigidity and resistance to elastic deformation, whereas the porosity represents voids and cavities within the composite materials. Excessive porosity can significantly reduce strength. The presence of voids can act as stress concentrators and promote crack initiation and propagation. So, high density and low porosity are desirable for achieving optimal mechanical properties.

Mechanical Properties

Effect of Varying CoCrFeMnNi HEA Content on the Hardness

The variation of hardness with the addition of reinforcement particles was depicted in Figure 8ii. A noticeable improvement in hardness was observed as HEA particles were added, with the hardness increasing regardless of HEA content. The maximum hardness achieved for the 8% HEA/AA composite was 28.57% higher than the base as-cast alloy. This improvement in hardness can be attributed to factors such as the fluidity of the molten metal, the density of dispersoids, the uniform dispersion of HEA particles within the aluminum matrix, and the solidification rate. The improved wettability between the metallic reinforcement and the aluminum matrix, as well as the interface between HEA particles and the aluminum matrix, enhances the material's resistance to indentation.

Table 5. Tensile Properties of Aluminum Alloys and Composites

S.No.	Composition	Hardness (HRB)	Yield stress (MPa)	Ultimate tensile stress (MPa)	% elongation
1.	AA 6082	71.330	112	174	14.2
2.	2% HEA/AA	80.387	165	234	13.1
3.	4% HEA/AA	85.689	188	289	11.3
4.	6% HEA/AA	82.368	185	273	8.4
5.	8% HEA/AA	89.714	204	327	7.6

Tensile Behavior

The relationship between the yield strength (Ys), ultimate tensile strength (UTS), and ductility (% elongation) with varying HEA reinforcements is depicted in Figure 8iii. It is apparent that the Ys and UTS exhibit similar behavior to hardness. As the reinforcement content increases, Ys and UTS both increase, whereas % elongation follows an opposing trend. Among the composites, the 4% HEA/AA composite exhibits the highest Ys and UTS values of 201 MPa and 327 MPa, respectively, which are a 79.46% and 87.931% improvement over the as-cast base alloy. The minimum values of Ys and UTS were reported for the 2% HEA/AA composite, at 165 MPa and 234 MPa, respectively. The % elongation of the as-cast alloy was 14.2%, which decreased with increasing reinforcement content and reached 7.6% for the 8% HEA/AA composite. The uniform dispersion of HEA particles in the 4% HEA/AA composite enables efficient accumulation of dislocations within the Al matrix, whereas HEA particle segregation in the 6% HEA/AA composite makes it more prone to brittle failure. However, the 8% HEA/AA composite exhibits improved strength due to back-stress hardening and dislocation hardening. The addition of HEA refines the grain structure, which impacts grain growth, leading to heterogeneous nucleation during solidification and an increase in grain number. In metal matrices, finer grain structures are associated with improved strength. The tensile properties of alloy and composites are listed in Table 5.

Tribological Behavior of Alloy and Composites

Dry Sliding Wear Attributes

Figure 9 depicts the rate of wear for the corresponding materials as the function of sliding distance (fixed 5000 meters) and normal applied pressure values of 0.25 MPa, 0.5 MPa, 0.75 MPa, 1.1 MPa, and 1.27 MPa, respectively. The obtained results revealed that an increase in wear is noticed with the sliding distance for all normal applied pressures. The as-cast AA 6082 alloy had the highest rate of wear among all compositions and normal applied pressures. On the other hand, the addition of HEA particles improved the wear resistance and reduced the wear rate.

The 8% HEA/AA composite had the lowest wear rate among all compositions and normal applied pressures. It is noteworthy to mention that the wear rate was almost constant in the initial sliding distance, but increased sharply after reaching the critical value, leading to a phenomenon known as the seizure. During the seizure, the material not only experiences loss of material but also adheres to the counter surface material. Chattering noise and high vibrations were reported at the seizure point. The as-cast AA6082 alloy gets seizure at a sliding distance of 4000 m and normal applied pressure of 0.75 MPa, with a corresponding wear rate of $6.788 \times 10^{-3} \text{ mm}^3/\text{m}$. Meanwhile, the 2% HEA/AA composite seized at a sliding distance of 5000 m and normal applied pressure of 0.75 MPa, with a corresponding wear rate of $5.31 \times 10^{-3} \text{ mm}^3/\text{m}$. The 8% HEA/AA composite seized at a sliding distance of 5000 m and normal applied pressure of 1.21 MPa, with a corresponding wear rate of $7.09 \times 10^{-3} \text{ mm}^3/\text{m}$.

Coefficient of Friction Visa-a-Vis Sliding Distance

Figure 10 depicts the evolution of the coefficient of friction as a function of sliding distance under various normal applied pressures of 0.25 MPa, 0.50 MPa, 0.76 MPa, 1.1 MPa, and 1.27 MPa, respectively. The trend of the coefficient of friction with sliding distance exhibits a zigzag pattern, making it challenging to deduce a clear conclusion from the observed trends. However, it can be observed that the as-cast AA6082 alloy exhibits the highest coefficient of friction, and the 8% HEA/AA composite exhibits the lowest coefficient of friction, regardless of the applied pressure. As the normal applied pressure increases, the values of the coefficient of friction converge. Beyond a critical sliding distance, the coefficient of friction suddenly increases, which marks the onset of the seizure. The as-cast AA6082 alloy experiences seizure at 0.75 MPa, where the coefficient of friction was reported as 0.53. Similarly, the 2% HEA/AA composite experiences seizure at 0.75 MPa with a corresponding coefficient of friction of 0.49. The 4% HEA/AA and 6% HEA/AA composites experience a seizure at 1.01 MPa with corresponding coefficients of friction of 0.58 and 0.56, respectively. The 8% HEA/AA composite experiences seizure at 1.27 MPa with a corresponding coefficient of friction of 0.61.

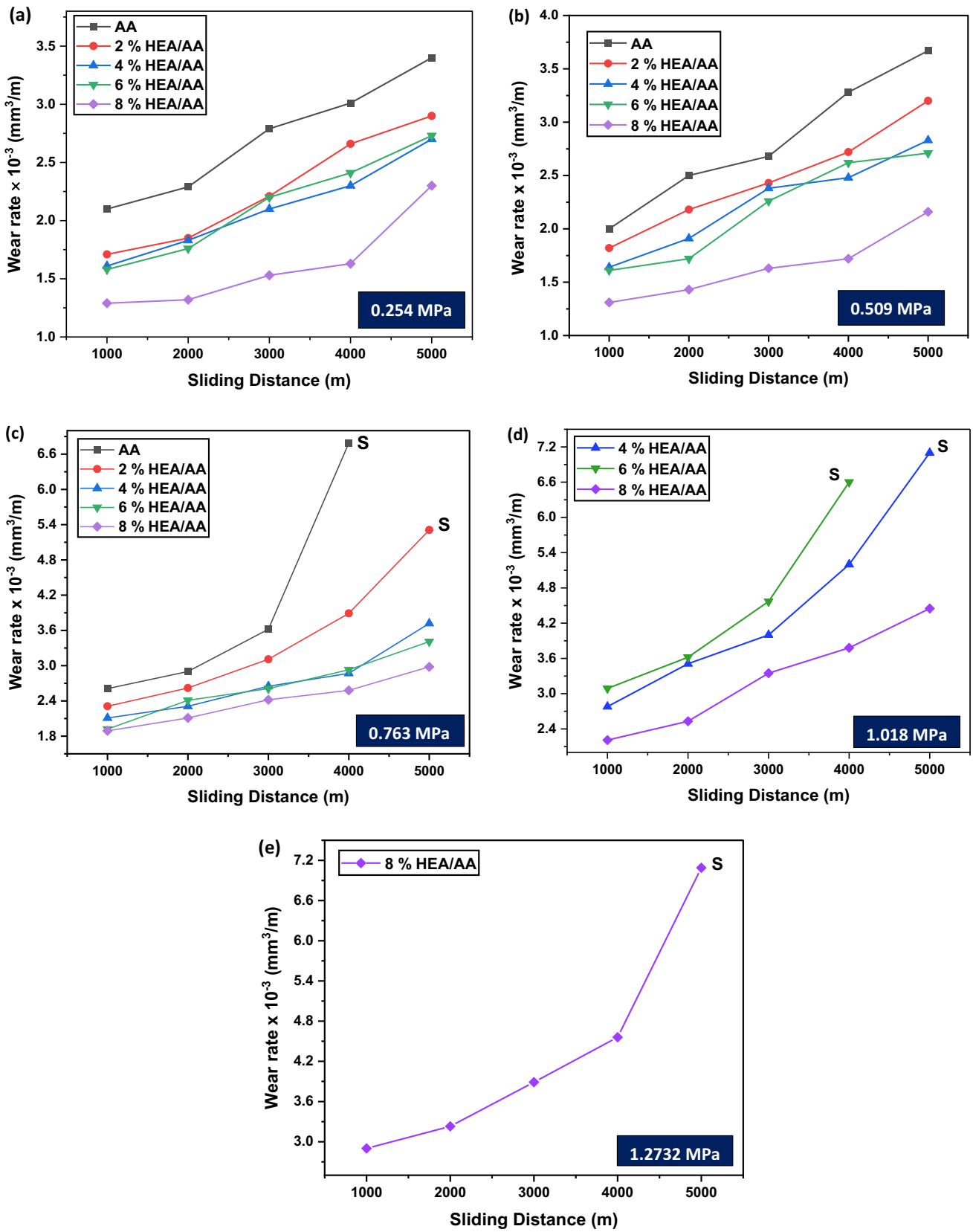


Figure 9. Wear rate corresponding to the sliding distance for different material compositions.

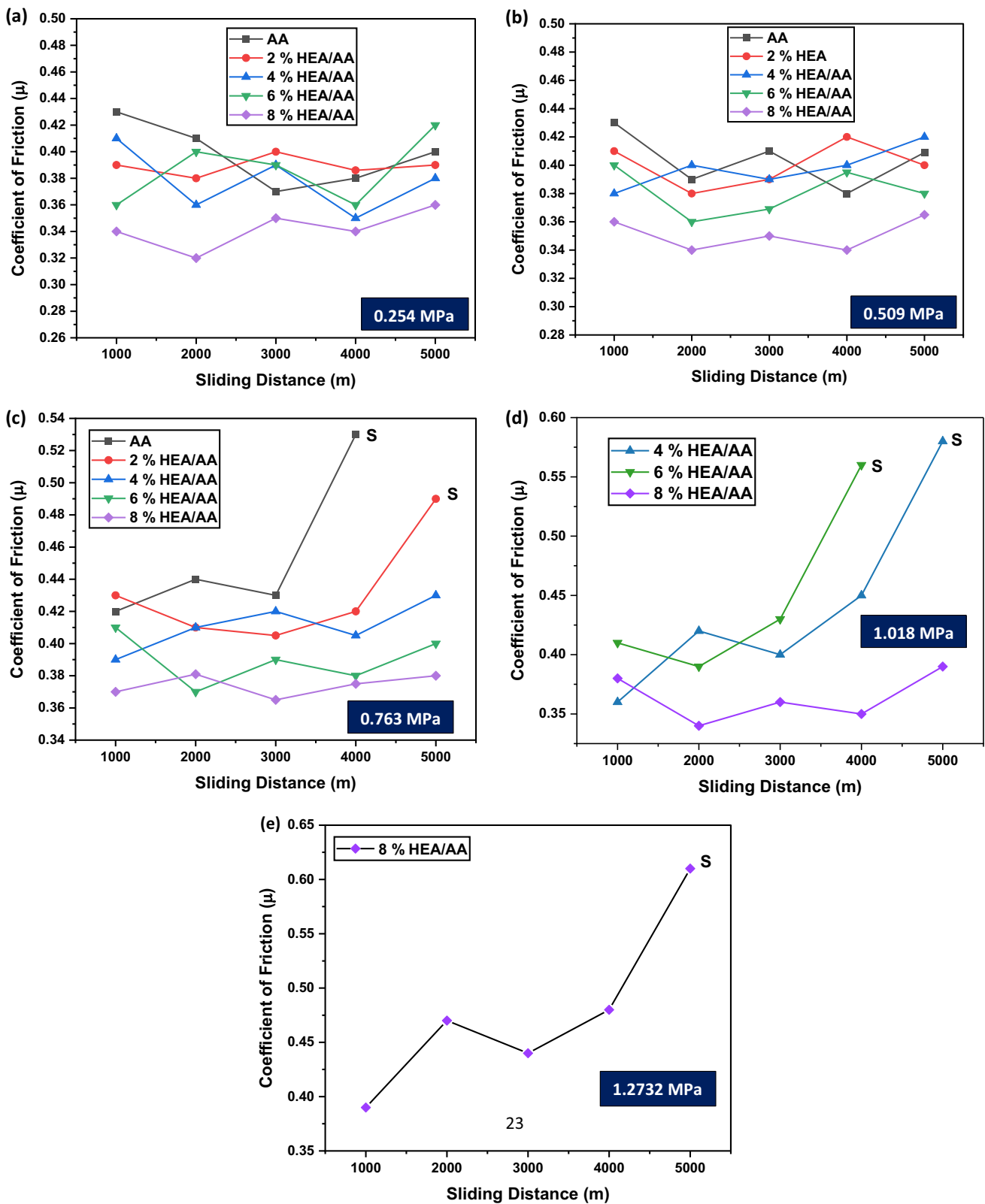


Figure 10. Variation of coefficient of friction with sliding distance for different material compositions.

Wear Coefficient vis-à-vis Applied Pressure

Figure 11 presents the correlation between the normal applied pressure and the wear coefficient. It was discovered

that as the normal applied pressure increases, a decline in the wear coefficient is observed for all composites. The as-cast AA 6082 alloy and the 2% HEA/AA composites were found to have seized at a normal applied pressure of 0.75

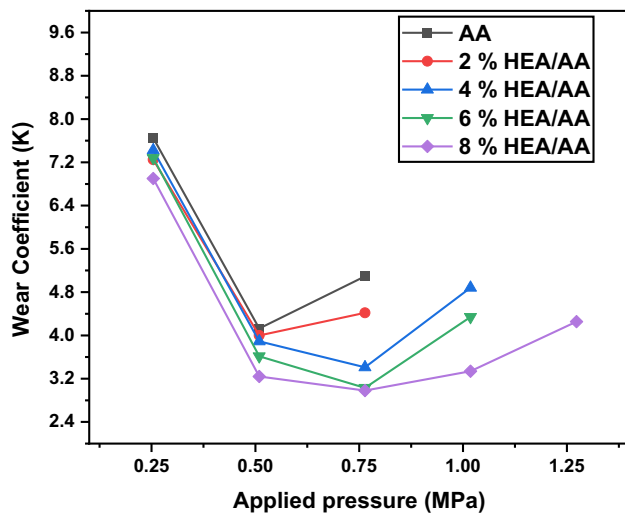


Figure 11. Variation of wear coefficient with normal applied pressure for different material compositions.

MPa, resulting in a marginal increase in the wear coefficient of the alloy from 4.13 to 5.09, while the wear coefficient of the 2% HEA/AA composite changed from 4.01 to 4.33.

For the 4% HEA/AA and 6% HEA/AA composites, a sharp decrease in the wear coefficient trend was noted, especially between the normal applied pressures of 0.25 MPa to 0.50 MPa. A further decrease was observed from 0.50 to 0.75 MPa, although at a slower rate. An increase in the wear coefficient was recorded for both composites as the normal applied pressure was increased from 0.75 to 1.00 MPa, with the corresponding wear coefficients at seizure being 4.88 and 4.33, respectively.

However, the wear coefficient for the 8% HEA/AA composite remained relatively constant between the normal applied pressures of 0.50 MPa to 1.1 MPa. The seizure for this composite was reported at 1.27 MPa, with the corresponding wear coefficient being 4.254.

Wear-Out Surface Analysis

In the wear sliding test, when surfaces come in contact, asperities to asperities contact occurred. In this work, softer aluminum asperities slide over harder steel asperities which grooves to form an aluminum surface. As the load increases which resulted in an increase in pressure at contact lead to deep grooves which can be visualized. At the intermediate pressure, grooves get deeper and more damage to the surface. It was evident that at high-pressure conditions initiation and propagation of cracks are more predominant. It is noteworthy to mention during sliding motion, with an increase in pressure cracks developed at the surface and propagate transversely and longitudinally. The transverse cracks meet the grooves and form small

debris at the worn surface. The AA 6082 gets seizure at 0.75 MPa, as the alloy experience intense frictional heat that is realized at higher pressure, the material gets softened and the micro weld is visualized more often at seizure condition severe damage surface with surface tearing and wear patches illustrates in Figure 12a, b.

For the 4% HEA/AA composition the seizure is observed at 1.01 MPa and is categorized by severe surface damage, surface tear, and development of parallel lips as shown in Figure 12c, d. For the 8% composite at lower pressure of 0.25 MPa grooves formation is not observed, and the wear surface is almost smooth with minute scratches. when the pressure reaches 0.75 MPa shallow grooves are observed. At this juncture, small debris can be observed. When the pressure reaches 1.25 MPa, the material gets seizure, and severe damage, as well as the parallel lips, can be seen in Figure 12d, e. Figure 12f–l reveals the different regions of worn surfaces at seizure conditions for 8% HEA/AA composite at the different parts of the wear surface.

The optical profilometer micrograph was utilized to analyze the worn surface of AA6082 alloy and HEA/AA composites which provides an overview of the wear behavior of alloy and composites illustrated in Figure 13. The wear surfaces have peaks and valleys which were developed due to loss of material during the sliding wear test and the intensity of wear was evaluated by average roughness. It is important to note as the HEA content increased wear resistant properties improved, as the specific wear rate decreased with HEA content.

Subsurface Analysis

The microstructural analysis of the subsurface of AA6082 and HEA/AA composites revealed three distinct regions: (1) the Undeformed Zone (UDZ), (2) the Plastically Deformed Zone (PDZ), and (3) the Mechanically Mixed Layer (MML). Figure 14a, b showed that at 0.763 MPa, the MML was observed to be approximately 91.4125 μm in thickness, with the PDZ measuring 69.983 μm . It was noted that crack initiation occurred at the intersection of the bulk UDZ and the severely deformed zone, which moved in the longitudinal direction and eventually transformed into MML over time. Further, sliding wear action caused the detachment of the MML and generated wear debris.

It was also noted that during the sliding motion, the grains of aluminum below the PDZ flowed along the direction of sliding. The subsurface of 2% HEA/AA subjected to seizure under normal applied pressure (0.763 MPa) was depicted in the micrograph (Figure 14c, d). Figure 14e, f shows two different zones of 4% HEA/AA composite, the bulk deformed zone, and the highly deformed zone. During the seizure, the MML was detached from the subsurface,

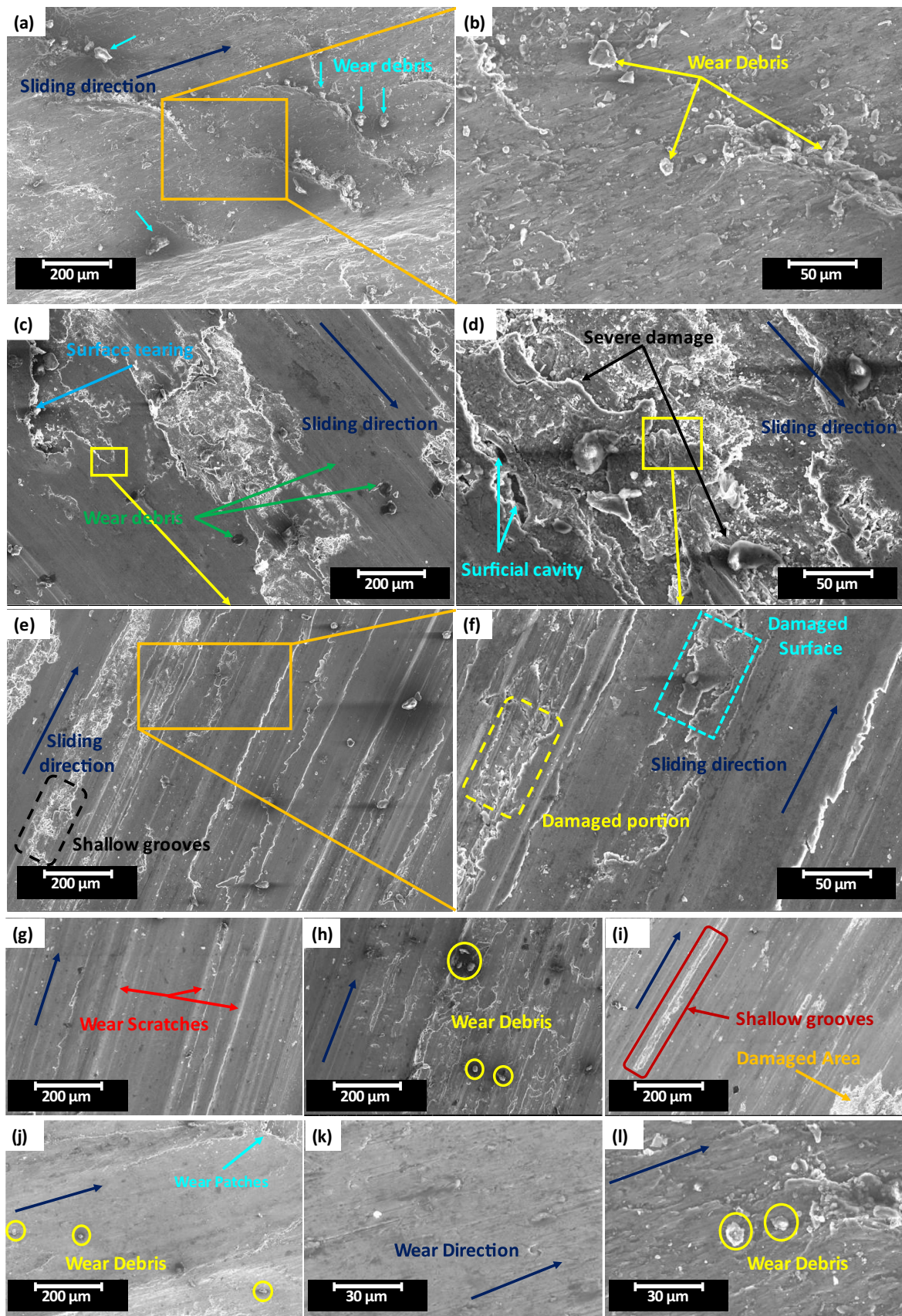


Figure 12. Low and high magnification wear micrographs with EDS graph (a, b) AA6082; (c, d) 4% HEA/AA; (d–i) 8% HEA/AA.

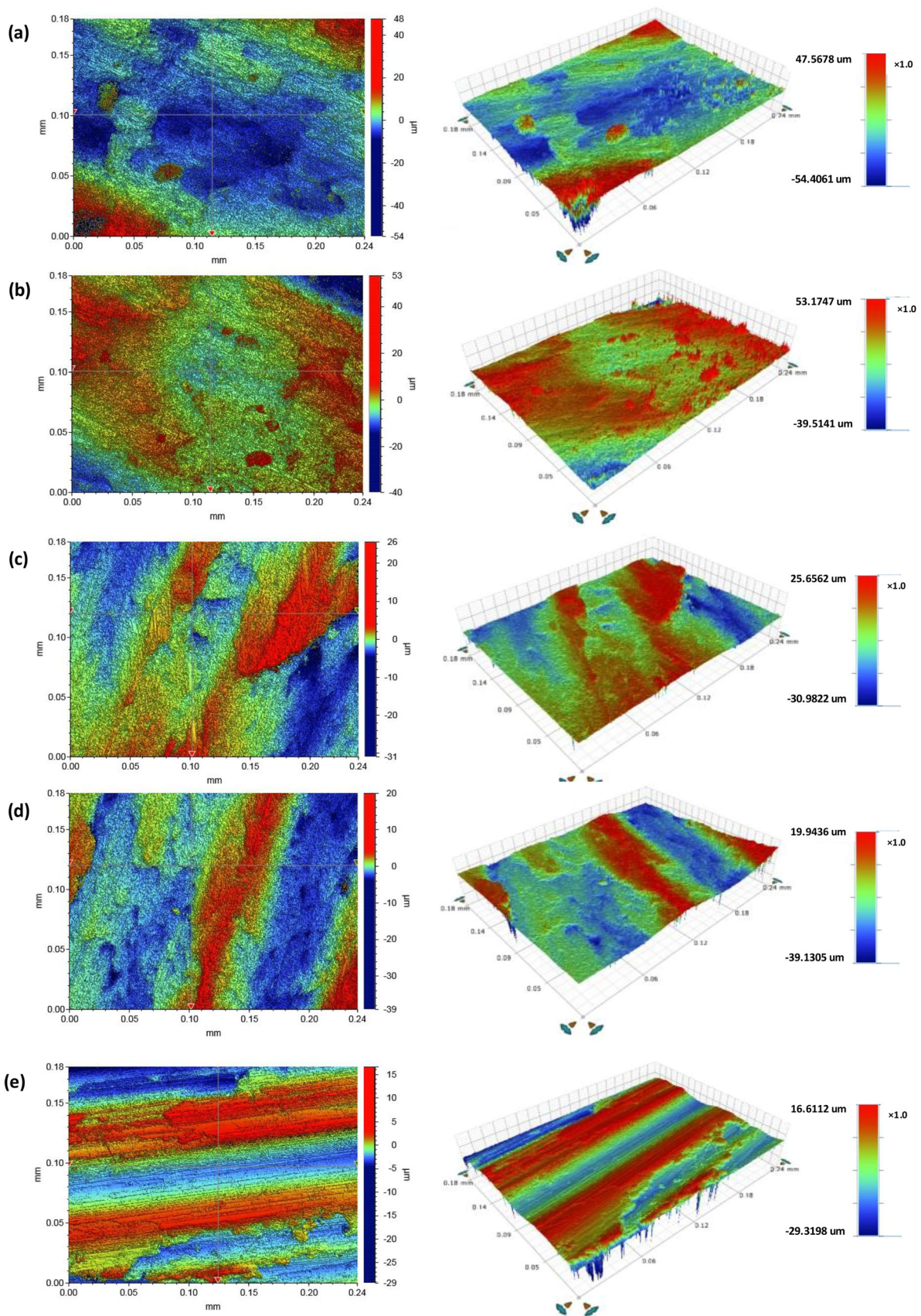


Figure 13. Optical profilometer micrographs for different material compositions at seizure: (a) AA 6082; (b) 2% HEA/AA composite; (c) 4% HEA/AA composite; (d) 6% HEA/AA composite; (e) 8% HEA/AA composite.

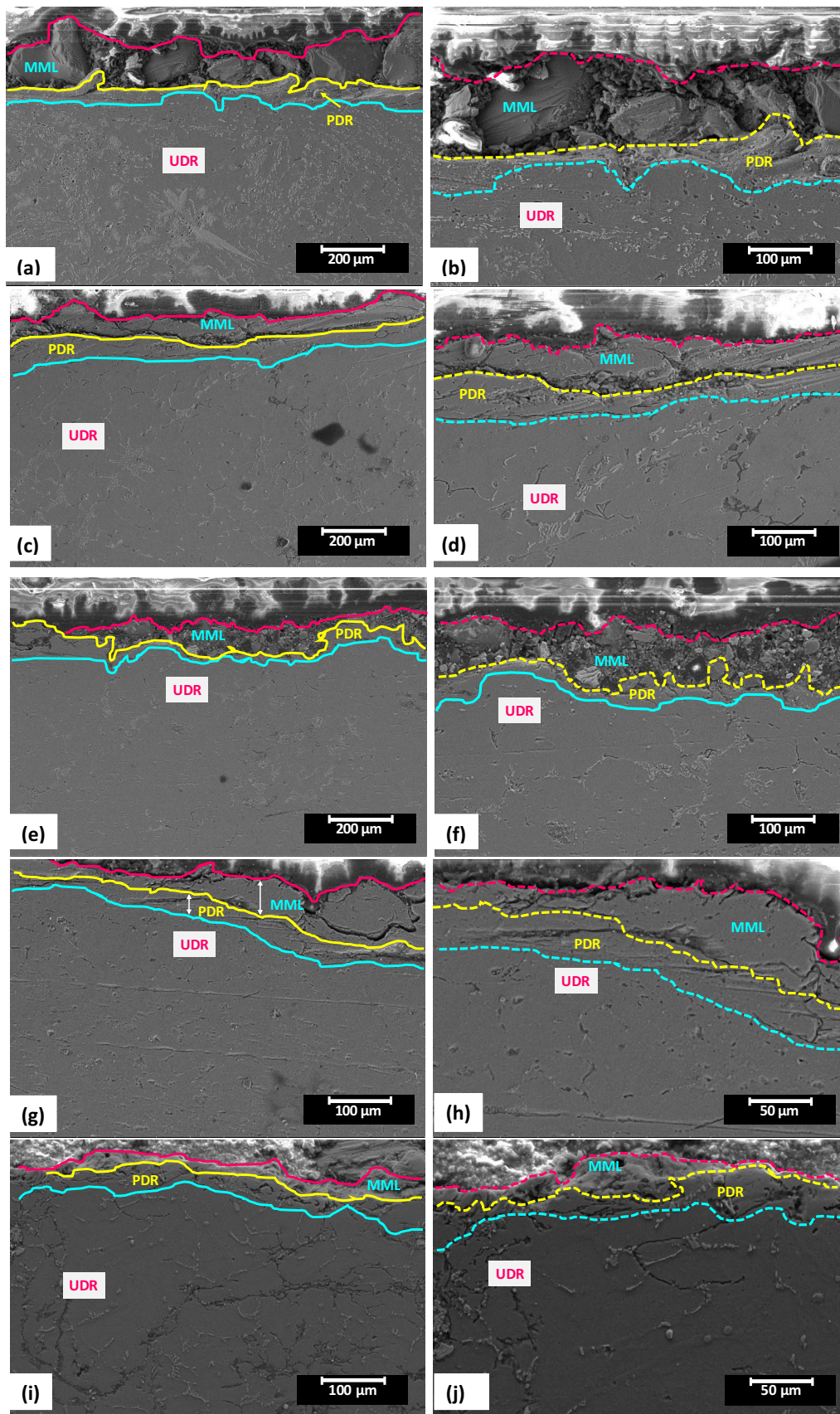


Figure 14. Lower and higher magnification micrograph images at seizure: (a) and (b) AA 6082 (MPa); (c) and (d) 2% HEA/AA (MPa); (e) and (f) 4% HEA/AA (MPa); (g) and (h) 6% HEA/AA (MPa); (i) and (j) 8% HEA/AA (MPa).

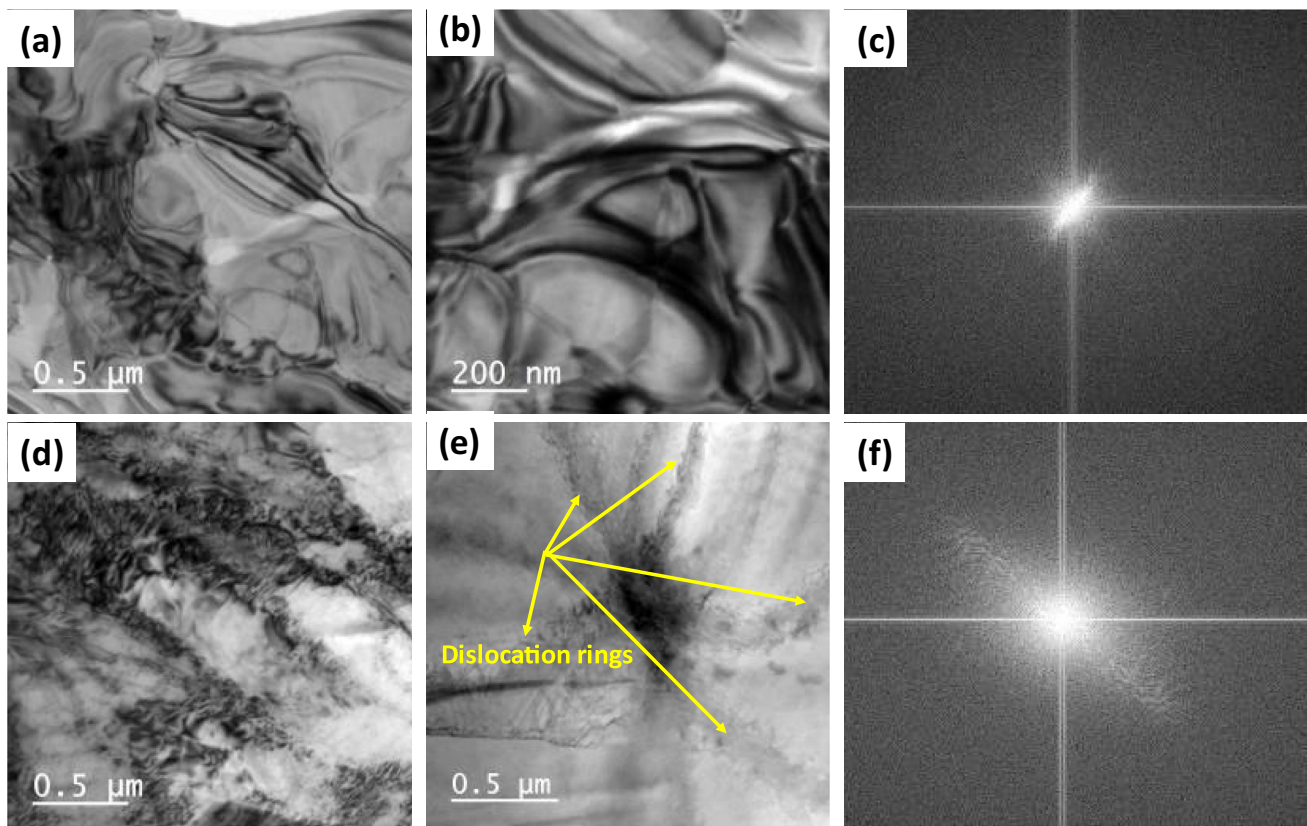


Figure 15. TEM images of dislocations evolved: (a) As-cast AA 6082, (b) high magnification image of as-cast AA 6082, (c) FFT of as-cast AA 6082, (d, e) 8% HEA/AA composite, and (f) FFT of 8% HEA/AA composite.

the thickness was reported as $61.3167 \mu\text{m}$ and the PDZ was evaluated as $39.814 \mu\text{m}$.

The research emphasized the nucleation and propagation of cracks, microstructure, and phase morphology of the different zones. Figures 14g, h represent the subsurface formation of the 6% HEA/AA composite at 1.018 MPa pressure, revealing an MML thickness of approximately $56.31 \mu\text{m}$ depth. The PDZ, measuring approximately $47.87 \mu\text{m}$, was found below the MML. It was noteworthy, at this stage, the HEA particles remained intact and no fragmentation of particles was observed in the MML. There was no observed particle pullout or debonding, which confirmed the good interfacial bonding between the HEA particles and the aluminum matrix. The 8% HEA/AA get seizure at 1.273 MPa, the composite underwent seizure and the MML ($30.416 \mu\text{m}$) transformed into the PDZ, as shown in Figure 14i, j. The plastically deformed zone extended up to $34.681 \mu\text{m}$ at 1.25 MPa

Discussions

Strengthening Mechanism Involved in Alloy and Composites

The addition of HEA particles to the Al matrix composite results in a significant enhancement of mechanical

properties at the minimal loss of ductility. The improved properties can be attributed to the strengthening mechanism of nano and sub-micron HEA reinforcement particles in the Al matrix. Figure 15e illustrates that when dislocations encounter undeformed HEA particles, they form dislocation rings around the particles. The accumulation of these dislocation rings imparts additional strength to the composite, as described in reference.⁴⁷ In various studies, it has been found that Orowan strengthening is dominant when the particles are dispersed throughout the grains. Dislocations travel from grain to grain boundary and the strength improvement from HEA particle hindrance near the grain boundaries are reduced, resulting in an increase in yield strength through Orowan strengthening, as described in reference.⁴⁸

The incorporation of HEA particles into an aluminum alloy matrix results in grain refinement, which can be divided into two categories: (1) HEA particles distributed at grain boundaries and (2) HEA particles at the liquid-solid interface that control solidification and act as heterogeneous nucleation sites, refining grains and increasing the grain count. The resulting finer grain structure leads to improved strength, toughness, and plasticity of the alloy, as described in reference.⁴⁹ The grain boundaries inhibit the movement of dislocations and facilitate the accumulation of dislocations near the grain boundaries, which is the

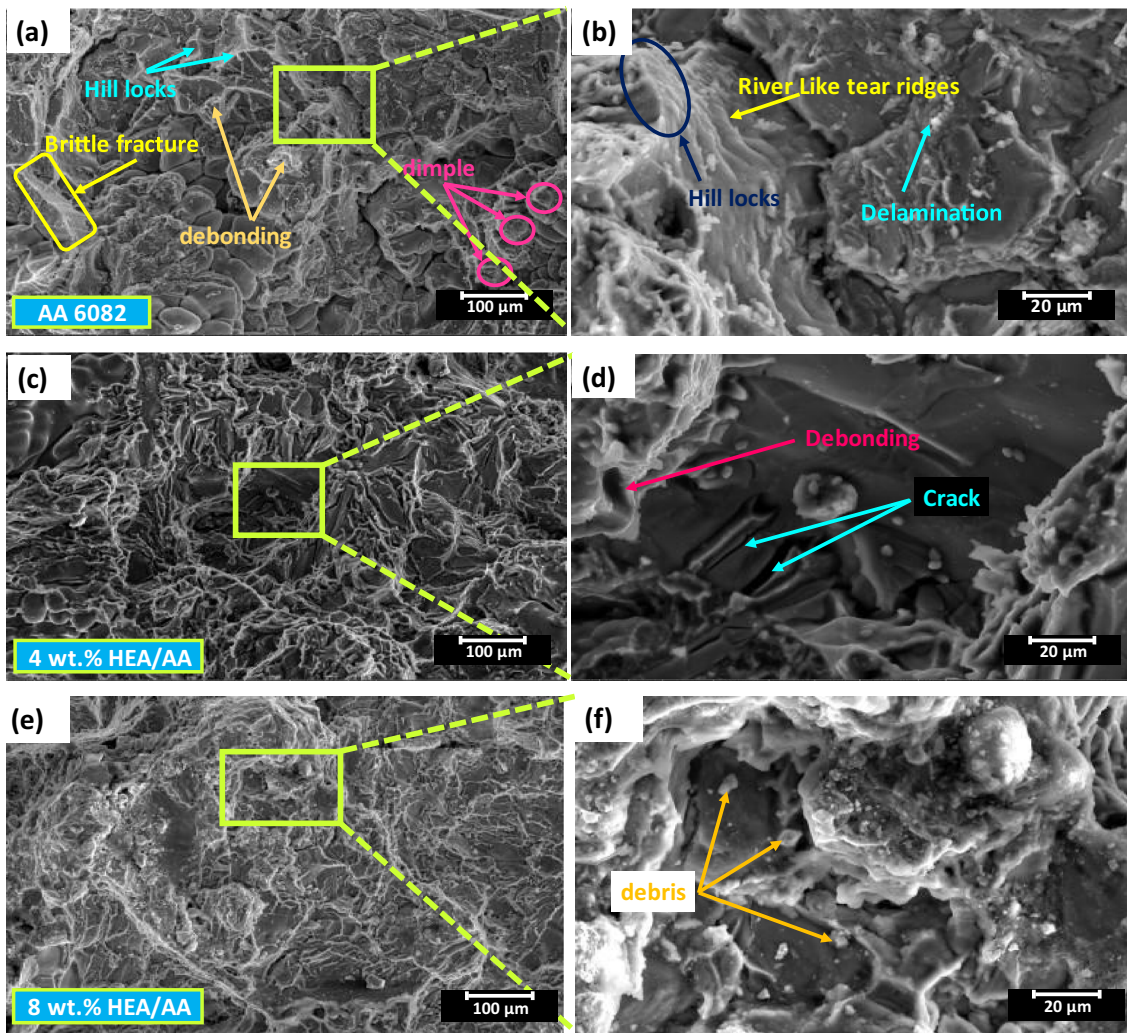


Figure 16. FESEM micrographs of fractured surfaces of as-cast alloy and composites.

primary factor contributing to the increased strength of alloys or composites.

The external load act on the materials leads to plastic deformation as the grains are finer load distributed uniformly and prevent or minimize stress concentration zone which resulted in better properties such as improved strength better plasticity and enhanced toughness.²

Governing Mechanism of Tensile Fracture

The illustration depicted in Figure 16 exhibits the morphological characteristics of the tensile fracture surfaces of Aluminum alloy and composites under as-cast conditions. The presence of river-like edges, hill-lock structures, and dimple-like morphologies suggest a ductile mode of fracture upon exposure to tensile stress. At a 4% HEA content, shallow dimple formations are prominently visible, while the characteristic tear ridge structure has been flattened. Additionally, the fracture surface displays evidence of two modes of HEA particle failure: brittle fracture and particle

pullout. These findings indicate the predominance of three modes of failure in HEA/AA composites, namely, (1) interfacial debonding between HEA particles and the Al matrix, (2) brittle failure of HEA particles, and (3) ductile failure of the Al matrix. It is noteworthy that, both the alloy and composites exhibit the same fracture mechanism, as opposed to undergoing a morphological transformation (e.g., from a plate-like structure to a spherical-type structure, as seen in Figure 16d).

Wear Rate

The 8% HEA/AA high entropy alloy composite exhibits superior resistance to wear and seizure compared to the base alloy. The improved wear resistance is attributed to the presence of hard particles that contribute to increased strength at elevated temperatures and provide plastic constraints. Furthermore, these hard particles act as projections that facilitate adhesion between the material and the counter surface of the hardened steel disk. It has been demonstrated that intermediate pressure during sliding

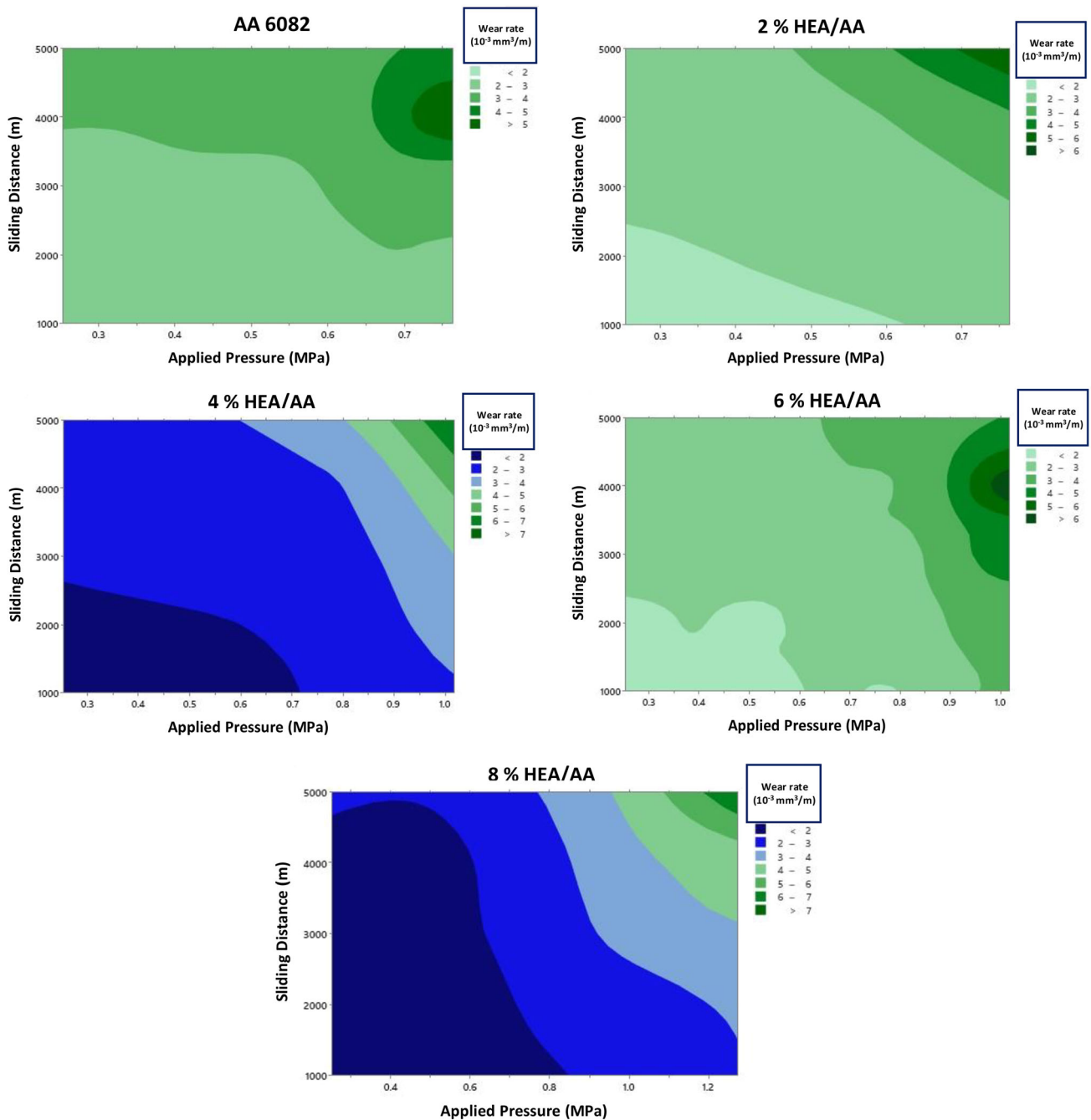


Figure 17. Wear map for normal applied pressure and sliding distance for AA 6082 and HEA/AA composites.

results in the formation of an oxide layer that causes oxidative wear. As pressure increases, a mechanically mixed layer is formed that eventually disintegrates, resulting in delaminating wear. Additionally, the presence of soft dispersoids acts as a lubricating agent, promoting the development of a lubricating film at the interface of the interacting regions, thus reducing friction and overall material loss.

Governing Wear Mechanism

During the sliding motion, the two interacting surfaces are exposed to both normal and shear loading. The contact between these surfaces, which are characterized by irregular asperities of varying shapes and sizes, leads to the piercing of the softer material's asperities by the harder ones, resulting in material loss. As the normal applied pressure increases, the harder asperities of the steel disk penetrate deeper into the asperities of the as-cast alloy and

Table 6. COF Corresponding to Normal Applied Pressure at Maximum Run Condition (up to 5000 m) for the Different Compositions

Pres.	Comp.				
	AA 6082	2% HEA/AA	4% HEA/AA	6% HEA/AA	8% HEA/AA
0.254 MPa	0.40	0.39	0.379	0.42	0.36
0.509 MPa	0.42	0.41	0.38	0.367	0.365
0.763 MPa	0.53 (S)	0.49 (S)	0.43	0.40	0.38
1.018 MPa	–	–	0.58 (S)	0.56 (S)	0.39
1.273 MPa	–	–	–	–	0.61 (S)

Bold values indicate the seizure condition achieves for the following composition at the requisite condition

composites, causing deformation and fracture of the softer surface asperities. It has been observed that up to a certain pressure, which varies depending on the composition, the wear rate follows a linear path. However, when the pressure exceeds this limit, excessive heat is generated, which increases the local adhesion between the mating surfaces. The heat-softened material experiences increased penetration of asperities, leading to significant wear. At this stage, weight loss due to delamination at the micro-cutting, fracture, and adhesion regions are prevalent. This results in the destruction of the mechanically mixed layer (MML) that forms at lower pressures. Beyond the critical pressure, the wear rate abruptly increases, changing from linear to a sharp increase. At low pressures, the pin surface asperities are sharper and stronger compared to those at high pressures, leading to deformation and fracture. In these low-pressure conditions, the healthy engagement between the asperities of the contacting surfaces is governed by the MML. It has been observed that the thickness of the MML in the unreinforced phase is thinner than in the reinforced phase.

Wear Map

The wear map depicted in Figure 17 provides a comprehensive representation of the synergistic influence of sliding distance and normal applied pressure on the wear rate of AA 6082 alloy and composites. The significance of the wear rate in relation to applied pressure and sliding distance is depicted via a color-coded scheme.

Coefficient of Friction

The initiation of metal-to-metal contact triggers abrasive wear and material loss regulation. The application of pressure may lead to the growth of an oxide layer due to frictional heating, elevating the temperature. This oxide layer functions as a lubricant film, inhibiting effective contact between the sliding surfaces, thereby accounting for the absence of a discernible rise in the coefficient of friction during the initial sliding runs. In the context of dry

sliding wear scenarios, two mechanisms often occur simultaneously, namely surface work hardening and fracture tendency. During the early stages of sliding, the soft Al surface undergoes work hardening, leading to increased efficiency over extended sliding distances.⁵⁰ Subsequent sliding will cause cracks to form and result in surface fracturing once the surface has been work-hardened. This causes fluctuations in the coefficient of friction (COF), which will be lower in cases of work hardening and greater in cases of fracturing. Both the AA 6082 alloy and composites exhibit this characteristic. In some instances, the COF is reported to remain essentially unchanged in relation to the sliding distance, potentially due to the balancing of the rates of hardening and fracturing. However, significant adhesion between opposing surfaces during seizure requires a greater amount of frictional energy to overcome the bonding, resulting in a dramatic increase in the COF during the seizure. The variation of COF with different normal applied pressure for maximum sliding distance i.e., up to 5000 meters, or the seizure condition achieved enlisted in Table 6.

Seizure Pressure

The correlation between the seizure pressure and the corresponding maximum pressure for various composites is depicted in the accompanying Figure 18. It is evident that the addition of HEA particles results in a noticeable increase in seizure pressure. The reinforcement content was observed to improve seizure resistance, with 2% HEA/AA exhibiting a seizure pressure of 0.763 MPa. Further increments in the reinforcement content to 4% HEA/AA and 6 HEA/AA led to observed seizure pressures of 1.018 MPa, demonstrating the positive effect of higher thermal stability on the composite. A substantial improvement in seizure resistance was observed for 8% HEA/AA.

Wear Coefficient

The prediction of the formation of wear debris, which is determined by the wear coefficient, can be quantified

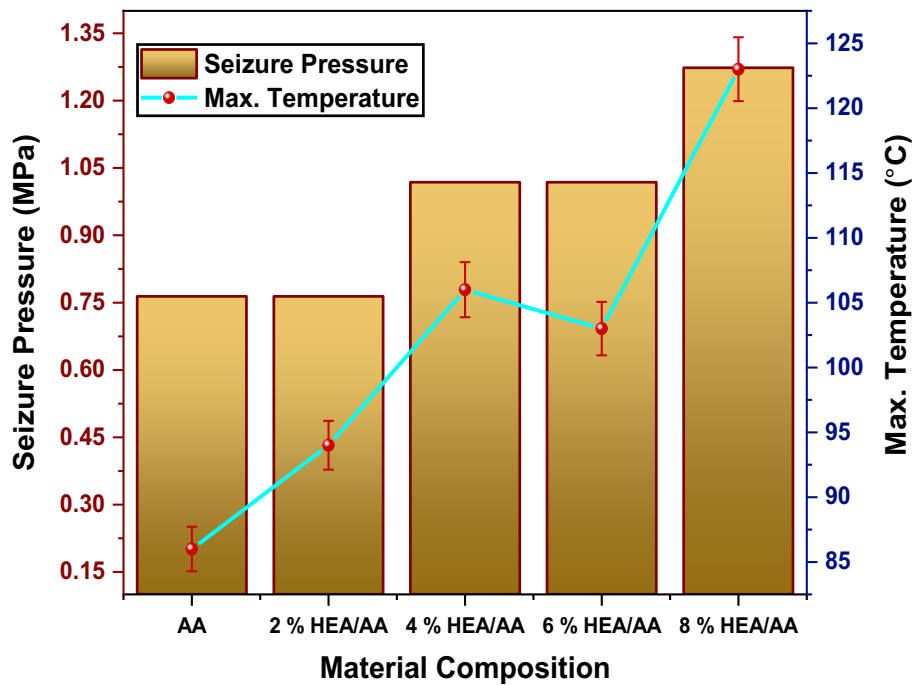


Figure 18. Variation of seizure pressure and maximum temperature corresponding to different materials.

Table 7. Wear Coefficient Corresponding to Normal Applied Pressure at Maximum Run Condition (up to 5000 m) for the Different Compositions

Pres.	Comp.				
	AA 6082	2% HEA/AA	4% HEA/AA	6% HEA/AA	8% HEA/AA
0.254 MPa	7.65	7.25	7.425	7.279	6.9
0.509 MPa	4.12875	4	3.89125	3.6131	3.24
0.763 MPa	5.09166 (S)	4.4175 (S)	3.41	3.03092	2.98
1.018 MPa	–	–	4.88125 (S)	4.33997 (S)	3.3375
1.273 MPa	–	–	–	–	4.254 (S)

Bold values indicate the seizure condition achieves for the following composition at the requisite condition

utilizing the equation $Q = KW/H$. From this equation, the wear coefficient can be determined and plotted against the applied pressure. It is observed that the wear coefficient remains relatively constant and fluctuates within a narrow range at intermediate applied pressure values. This constant value of the wear coefficient indicates that the likelihood of the formation of wear debris remains consistent. It has been established that the wear coefficient (i.e., the probability of wear debris formation) is proportional to the hardness of the materials and inversely proportional to the applied pressure. When the pressure is elevated, the material becomes more susceptible to deformation, leading to strain hardening of the surface and reducing the possibility of debris formation. Conversely, for harder materials, the tendency toward fracture increases, thus resulting in greater wear debris formation. The variation of wear coefficient with different normal applied pressure for maximum

sliding distance i.e., up to 5000 meters or the seizure condition achieved enlisted in Table 7.

Conclusions

In the present study, the influence of varying HEA content on the mechanical and tribological properties was studied and the following conclusion was drawn from the investigation:

- The CoCrFeMnNi HEA were prepared via mechanical alloying technique, that successfully used as the reinforcing agent to develop aluminum metal matrix composites utilizing stir squeeze casting.
- The OM and FESEM micrograph revealed that fairly enough even dispersion of HEA particles

was observed in AMCs. The elemental concentration was confirmed by EDX analysis, whereas the presence of different elements and phases was confirmed by XRD analysis. TEM was used to study the dislocations lattice structure of AMCs along with the morphology of HEA particles.

- Hardness and tensile strength improved with the addition of HEA particles and maximum values were reported for 8% HEA/AA as 89.714 HRB, and 327 MPa, respectively, while ductility was observed to decrease and % elongation tends to decrease from 14.2 to 7.6% from alloy to 8% HEA/AA composite.
- The worn surface morphology and specific wear rate indicate that irrespective of HEA content composite exhibits superior wear resistance properties than the monolithic alloy.
- The variation of temperature with sliding distance eventually in the same manner as the wear rate for all normal applied pressure.
- The seizure resistance of 8% HEA/AA was significantly enhanced over monolithic AA 6082 by 66.86%.
- The worn surface includes damaged patches, wear debris, and tiny grooves under low normal applied pressure, whereas parallel ridges, surface tearing, and heavily damaged surfaces were observed during the seizure conditions.
- The composite exhibits a lower wear rate with the inclusion of HEA particles. It was observed that as the normal applied pressure increased, as the normal applied pressure increased up to a certain limit, material loss abruptly increased during the seizure condition.

Acknowledgements

The research work is carried out at Maulana Azad National Institute of Technology, Bhopal, and supported by the Ministry of Education, Government of India. The authors are very grateful to the Indian Institute of Technology, Roorkee, and the Indian Institute of Technology, Kanpur for their assistance.

Funding

No funding is available.

Data availability

All data generated or analyzed during this study are included in this published article.

Conflict of interest The authors declare that they have no known competing financial interests or personal relationships that could have appeared to influence the work reported in this paper.

REFERENCES

1. J. Zhang, S. Yang, Z. Chen, H. Wu, J. Zhao, Z. Jiang, Graphene encapsulated SiC nanoparticles as tribology-favoured nanofillers in aluminium composite. *Compos. Part B Eng.* **162**, 445–453 (2019). <https://doi.org/10.1016/j.compositesb.2018.12.046>
2. H. Yang, L. Jiang, M. Balog, P. Krizik, J.M. Schoenung, Reinforcement size dependence of load bearing capacity in ultrafine-grained metal matrix composites. *Metall. Mater. Trans. A Phys. Metall. Mater. Sci.* **48**(9), 4385–4392 (2017). <https://doi.org/10.1007/s11661-017-4186-7>
3. P. Kumar et al., Effect of eutectic silicon and silicon carbide particles on high stress scratching wear of aluminium composite for various testing parameters. *Wear* **482–483**, 203921 (2021). <https://doi.org/10.1016/j.wear.2021.203921>
4. R. Vasanth Kumar, R. Keshavamurthy, C.S. Perugu, M. Alipour, C. Siddaraju, Influence of hot rolling on friction and wear behaviour of Al6061-ZrB₂ in-situ metal matrix composites. *J. Manuf. Process.* **69**, 473–490 (2021). <https://doi.org/10.1016/j.jmapro.2021.07.058>
5. V. Singhal, O.P. Pandey, Dry sliding wear study of solid lubricants and sillimanite-reinforced aluminum alloy composites. *J. Mater. Eng. Perform.* **30**(11), 8369–8384 (2021). <https://doi.org/10.1007/s11665-021-05975-y>
6. M. Sivanesh Prabhu, A. Elaya Perumal, S. Arulvel, R. Franklin Issac, Friction and wear measurements of friction stir processed aluminium alloy 6082/CaCO₃ composite. *Meas. J. Int. Meas. Confed.* **142**, 10–20 (2019). <https://doi.org/10.1016/j.measurement.2019.04.061>
7. U. Devadiga, R.K.R. Poojary, P. Fernandes, Artificial neural network technique to predict the properties of multiwall carbon nanotube-fly ash reinforced aluminium composite. *J. Mater. Res. Technol.* **8**(5), 3970–3977 (2019). <https://doi.org/10.1016/j.jmrt.2019.07.005>
8. M.M. Castro et al., A magnesium–aluminium composite produced by high-pressure torsion. *J. Alloys Compd.* **804**, 421–426 (2019). <https://doi.org/10.1016/j.jallcom.2019.07.007>
9. R. Vignesh Kumar, R. Harichandran, U. Vignesh, M. Thangavel, S.B. Chandrasekhar, Influence of hot extrusion on strain hardening behaviour of graphene platelets dispersed aluminium composites. *J. Alloys Compd.* **855**, 157448 (2021). <https://doi.org/10.1016/j.jallcom.2020.157448>
10. C. Fenghong, C. Chang, W. Zhenyu, T. Muthuramalingam, C. Chang, Effects of silicon carbide and tungsten carbide in aluminium metal matrix composites. *SILICON* **11**, 2625–2632 (2019)

11. K. Nithesh, M.C. Gowrishankar, R. Nayak, S. Sharma, Effect of light weight reinforcement and heat treatment process parameters on morphological and wear aspects of hypoeutectic Al–Si based composites—a critical review. *J. Mater. Res. Technol.* **15**, 4272–4292 (2021). <https://doi.org/10.1016/j.jmrt.2021.10.019>
12. S. Liu, Y. Wang, T. Muthuramalingam, G. Anbu-chezhiyan, Effect of B₄C and MOS₂ reinforcement on micro structure and wear properties of aluminum hybrid composite for automotive applications. *Compos. Part B* **176**, 107329 (2019). <https://doi.org/10.1016/j.compositesb.2019.107329>
13. S. Arif, B. Jamil, M. Bilal, N. Shaikh, T. Aziz, A.H. Ansari, Characterization of surface morphology, wear performance and modelling of graphite reinforced aluminium hybrid composites. *Eng. Sci. Technol. an Int. J.* **23**(3), 674–690 (2020). <https://doi.org/10.1016/j.jestch.2019.07.001>
14. M. Wu, R.C. Setiawan, D.Y. Li, Benefits of passive element Ti to the resistance of AlCrFeCoNi high-entropy alloy to corrosion and corrosive wear. *Wear* (2022). <https://doi.org/10.1016/j.wear.2021.204231>
15. J. Ren et al., Strong yet ductile nanolamellar high-entropy alloys by additive manufacturing. *Nature* **608**(7921), 62–68 (2022). <https://doi.org/10.1038/s41586-022-04914-8>
16. A. Kumar, A. Singh, A. Suhane, A critical review on mechanically alloyed high entropy alloys: processing challenges and properties. *Mater. Res. Express* (2022). <https://doi.org/10.1088/2053-1591/ac69b3>
17. J.W. Yeh et al., Nanostructured high-entropy alloys with multiple principal elements: Novel alloy design concepts and outcomes. *Adv. Eng. Mater.* **6**(5), 299–303 (2004). <https://doi.org/10.1002/adem.200300567>
18. B. Cantor, I.T.H. Chang, P. Knight, A.J.B. Vincent, Microstructural development in equiatomic multi-component alloys. *Mater. Sci. Eng. A* **375–377**, 213–218 (2004). <https://doi.org/10.1016/j.msea.2003.10.257>
19. F. Otto, Y. Yang, H. Bei, E.P. George, Relative effects of enthalpy and entropy on the phase stability of equiatomic high-entropy alloys. *Acta Mater.* **61**(7), 2628–2638 (2013). <https://doi.org/10.1016/j.actamat.2013.01.042>
20. B. Schuh et al., Mechanical properties, microstructure and thermal stability of a nanocrystalline CoCr-FeMnNi high-entropy alloy after severe plastic deformation. *Acta Mater.* **96**, 258–268 (2015). <https://doi.org/10.1016/j.actamat.2015.06.025>
21. X. Gao, Y. Lu, Laser 3D printing of CoCrFeMnNi high-entropy alloy. *Mater. Lett.* **236**, 77–80 (2019). <https://doi.org/10.1016/j.matlet.2018.10.084>
22. Y. Chew et al., Microstructure and enhanced strength of laser aided additive manufactured CoCrFeNiMn high entropy alloy. *Mater. Sci. Eng. A* **744**, 137–144 (2019). <https://doi.org/10.1016/j.msea.2018.12.005>
23. K. Praveen Kumar, M. Gopi Krishna, J. Babu Rao, N.R.M.R. Bhargava, Fabrication and characterization of 2024 aluminium–high entropy alloy composites. *J. Alloys Compd.* **640**, 421–427 (2015). <https://doi.org/10.1016/j.jallcom.2015.03.093>
24. J. Li et al., Friction stir processing of high-entropy alloy reinforced aluminum matrix composites for mechanical properties enhancement. *Sci. Eng. A* **792**, 139755 (2020). <https://doi.org/10.1016/j.msea.2020.139755>
25. A. Kumar, A. Singh, A. Suhane, Synthesis and characterization of a novel CoCrFeMnNi high-entropy alloy-reinforced AA6082 composite. *J. Mater. Res.* (2022). <https://doi.org/10.1557/s43578-022-00701-3>
26. D. Sun et al., High-temperature oxidation and wear properties of TiC-reinforced CrMnFeCoNi high entropy alloy composite coatings produced by laser cladding. *Surf. Coat. Technol.* **438**, 128407 (2022). <https://doi.org/10.1016/j.surfcoat.2022.128407>
27. A. Zhang, J. Han, B. Su, J. Meng, A novel CoCrFeNi high entropy alloy matrix self-lubricating composite. *J. Alloys Compd.* **725**, 700–710 (2017). <https://doi.org/10.1016/j.jallcom.2017.07.197>
28. A.K. Singh, S. Soni, R.S. Rana, Wear mechanism maps for stir-squeeze cast AA7068 Alloy/ZrO_{2p} composite in accordance with normal load versus sliding speed diagram. *Trans. Indian Inst. Met.* **75**(11), 2867–2874 (2022). <https://doi.org/10.1007/s12666-022-02662-x>
29. P. Han et al., Friction stir processing of cold-sprayed high-entropy alloy particles reinforced aluminum matrix composites: corrosion and wear properties. *Met. Mater. Int.* **29**(3), 845–860 (2023). <https://doi.org/10.1007/s12540-022-01248-y>
30. A.K. Singh, S. Soni, R.S. Rana, Sliding wear response of ultrasonic-assisted stir-squeeze cast Al-Zn(-Mg) alloy/ZrO_{2p} composite: wear mechanism and subsurface deformation. *Surf. Topogr. Metrol. Prop.* **10**(2), 025020 (2022). <https://doi.org/10.1088/2051-672X/ac6f71>
31. M. Arif Mahmood, F. Ghassan Alabtah, Y. Al Hamidi, M. Khraisheh, On laser additive manufacturing of high-entropy alloys: a critical assessment of in-situ monitoring techniques and their suitability. *Mater. Des.* **226**, 111658 (2023). <https://doi.org/10.1016/j.matdes.2023.111658>
32. Z. Savaedi, R. Motallebi, H. Mirzadeh, A review of hot deformation behavior and constitutive models to predict flow stress of high-entropy alloys. *J. Alloys Compd.* **903**, 163964 (2022). <https://doi.org/10.1016/j.jallcom.2022.163964>
33. F.D.C. Garcia Filho, R.O. Ritchie, M.A. Meyers, S.N. Monteiro, Cantor-derived medium-entropy alloys: bridging the gap between traditional metallic and high-entropy alloys. *J. Mater. Res. Technol.* **17**, 1868–1895 (2022). <https://doi.org/10.1016/j.jmrt.2022.01.118>

34. A. Kumar, A. Singh, A. Suhane, Mechanically alloyed high entropy alloys: existing challenges and opportunities. *J. Mater. Res. Technol.* **17**, 2431–2456 (2022). <https://doi.org/10.1016/j.jmrt.2022.01.141>
35. X. Duan et al., Cooperative effect of Cr and Al elements on passivation enhancement of eutectic high-entropy alloy AlCoCrFeNi_{2.1} with precipitates. *J. Mater. Sci. Technol.* **136**, 97–108 (2023). <https://doi.org/10.1016/j.jmst.2022.07.023>
36. N. Kumar, M.D.K.S.S. Sharma, B.R. Kamath, Sliding wear behaviour of nickel-coated short fibre-reinforced Al7075 composites. *J. Fail. Anal. Prev.* **20**(5), 1609–1614 (2020). <https://doi.org/10.1007/s11668-020-00955-1>
37. A. Coyal, N. Yuvaraj, R. Butola, L. Tyagi, An experimental analysis of tensile, hardness and wear properties of aluminium metal matrix composite through stir casting process. *SN Appl. Sci.* **2**(5), 1–10 (2020). <https://doi.org/10.1007/s42452-020-2657-8>
38. H. Hanizam, M.S. Salleh, M.Z. Omar, A.B. Sulong, Optimisation of mechanical stir casting parameters for fabrication of carbon nanotubes-aluminium alloy composite through Taguchi method. *J. Mater. Res. Technol.* **8**(2), 2223–2231 (2019). <https://doi.org/10.1016/j.jmrt.2019.02.008>
39. V. Pandian, S. Kannan, Processing and preparation of aerospace-grade aluminium hybrid metal matrix composite in a modified stir casting furnace integrated with mechanical supersonic vibration squeeze infiltration method. *Mater. Today Commun.* **26**, 101732 (2021). <https://doi.org/10.1016/j.mtcomm.2020.101732>
40. S.D. Kumar, M. Ravichandran, A. Jeevika, B. Stalin, C. Kailasanathan, A. Karthick, Effect of ZrB₂ on microstructural, mechanical and corrosion behaviour of aluminium (AA7178) alloy matrix composite prepared by the stir casting route. *Ceram. Int.* **47**(9), 12951–12962 (2021). <https://doi.org/10.1016/j.ceramint.2021.01.158>
41. G. Wang et al., Synthesis and thermal stability of a nanocrystalline MoNbTaTiV refractory high-entropy alloy via mechanical alloying. *Int. J. Refract. Met. Hard Mater.* (2019). <https://doi.org/10.1016/j.ijrmhm.2019.104988>
42. Y.L. Chen, Y.H. Hu, C.A. Hsieh, J.W. Yeh, S.K. Chen, Competition between elements during mechanical alloying in an octonary multi-principal-element alloy system. *J. Alloys Compd.* **481**(1–2), 768–775 (2009). <https://doi.org/10.1016/j.jallcom.2009.03.087>
43. M. Huang, J. Jiang, Y. Wang, Y. Liu, Y. Zhang, Effects of milling process parameters and PCAs on the synthesis of Al_{0.8}Co_{0.5}Cr_{1.5}CuFeNi high entropy alloy powder by mechanical alloying. *Mater. Des.* **217**, 110637 (2022). <https://doi.org/10.1016/j.matdes.2022.110637>
44. Y.L. Liu, S.B. Kang, H.W. Kim, Complex microstructures in an as-cast Al–Mg–Si alloy. *Mater. Lett.* **41**(6), 267–272 (1999). [https://doi.org/10.1016/S0167-577X\(99\)00141-X](https://doi.org/10.1016/S0167-577X(99)00141-X)
45. M. Warmuzek, K. Rabczak, J. Sieniawski, The course of the peritectic transformation in the Al-rich Al–Fe–Mn–Si alloys. *J. Mater. Process. Technol.* **162–163**, 422–428 (2005). <https://doi.org/10.1016/j.jmatprotec.2005.02.030>
46. M. Warmuzek, J. Sieniawski, K. Wicher, G. Mrówka, The study of the distribution of the transition metals and Si during primary precipitation of the intermetallic phases in Al–Mn–Si alloys. *J. Mater. Process. Technol.* **175**(1–3), 421–426 (2006). <https://doi.org/10.1016/j.jmatprotec.2005.04.005>
47. J. George, E. Dieter, *Mechanical metallurgy* (McGraw-Hill Book Company, Inc, New York, 1961), pp.3–609
48. K.B. Nie, X.J. Wang, K. Wu, X.S. Hu, M.Y. Zheng, Development of SiCp/AZ91 magnesium matrix nanocomposites using ultrasonic vibration. *Mater. Sci. Eng. A* **540**, 123–129 (2012). <https://doi.org/10.1016/j.msea.2012.01.112>
49. S.F. Hassan, M. Gupta, Effect of particulate size of Al₂O₃ reinforcement on microstructure and mechanical behavior of solidification processed elemental Mg. *J. Alloys Compd.* **419**(1–2), 84–90 (2006). <https://doi.org/10.1016/j.jallcom.2005.10.005>
50. A.K. Singh, S. Soni, R.S. Rana, Mechanical and sliding wear behavior of stir-squeeze cast and T6 heat-treated AA7068-ZrO_{2p} composite. *Compos. Interfaces* **00**(00), 1–27 (2022). <https://doi.org/10.1080/09276440.2022.2120736>

Publisher's Note Springer Nature remains neutral with regard to jurisdictional claims in published maps and institutional affiliations.

Springer Nature or its licensor (e.g. a society or other partner) holds exclusive rights to this article under a publishing agreement with the author(s) or other rightsholder(s); author self-archiving of the accepted manuscript version of this article is solely governed by the terms of such publishing agreement and applicable law.